Raub, C., Bohnhoff, M., Petrovic, B., Parolai, S., Malin, P., Yanik, K., Kartal, R. F., Kiliç, T. (2016): Seismic-Wave Propagation in Shallow Layers at the GONAF-Tuzla Site, Istanbul, Turkey. - *Bulletin of the Seismological Society of America*, *106*, 3, pp. 912—927.

DOI: http://doi.org/10.1785/0120150216

THE SEISMOLOGICAL SOCIETY OF AMERICA
400 Evelyn Ave., Suite 201
Albany, CA 94706-1375
(510) 525-5474; FAX (510) 525-7204
www.seismosoc.org

Bulletin of the Seismological Society of America, Vol. 106, No. 3, pp. 912–927, June 2016, doi: 10.1785/0120150216

Ⓔ

Seismic-Wave Propagation in Shallow Layers at the GONAF-Tuzla Site, Istanbul, Turkey

by Christina Raub, Marco Bohnhoff,* Bojana Petrovic, Stefano Parolai, Peter Malin, Kenan Yanik, Recai Feyiz Kartal, and Tuğbay Kiliç

Abstract Using the first dataset available from the downhole Geophysical Observatory of the North Anatolian Fault, we investigated near-surface seismic-wave propagation on the Tuzla Peninsula, Istanbul, Turkey. We selected a dataset of 26 seismograms recorded at Tuzla at sensor depths of 0, 71, 144, 215, and 288 m. To determine near-surface velocities and attenuation structures, the waveforms from all sensors were pairwise deconvolved and stacked. This produced low-noise empirical Green's functions for each borehole depth interval. From the Green's functions, we identified reflections from the free surface and a low-velocity layer between ∼90 and ∼140 m depth. The presence of a low-velocity zone was also confirmed by a sonic log run in the borehole. This structure, plus high near-surface *P*- and *S*-wave velocities of ∼3600–4100 and ∼1800 m/s, lead to complex interference effects between upgoing and downgoing waves. As a result, the determination of quality factors (Q) with standard spectral ratio techniques was not possible. Instead, we forward modeled the Green's functions in the time domain to determine effective Q values and to refine our velocity estimates. The effective Q_P values for the depth intervals of 0–71, 0–144, 0–215, and 0–288 m were found to be 19, 35, 39, and 42, respectively. For the S waves, we obtained an effective Q_S of 20 in the depth interval of 0–288 m. Considering the assumptions made in our modeling approach, it is evident that these effective quality factors are biased by impedance contrasts between our observation points. Our results show that, even after correcting for a free-surface factor of 2, the motion at the surface was found to be 1.7 times greater than that at 71 m depth. Our efforts also illustrate some of the difficulties of dealing with site effects in a strongly heterogeneous subsurface.

Online Material: Plots of resistivity and caliper logs and the spectra of all 26 events.

Introduction

For numerous scientific applications such as earthquake source parameter studies (e.g., Hauksson *et al.*, 1987; Abercrombie and Leary, 1993), it is important to quantify how near-surface geologic structures influence the waveforms and amplitudes of seismic waves. Shallow subsurface geologic features affect the seismic wavefield through amplification due to near-surface low-impedance layers, resonance effects caused by strong impedance contrasts, high-frequency attenuation due to scattering, and intrinsic attenuation. Studies of these effects are usually based on a two-geographical-location comparison method. A common practice is to compare recordings from the site of interest to those from a close-by reference station (preferably one installed on outcropping bedrock or in a deep borehole), the optimum being a vertical array of seismometers from the surface down to competent rock (Steidl *et al.*, 1996). In the latter circumstance and with a sufficient number of sensors, the mechanical properties of the soil can be measured directly for different depth intervals.

Such an arrangement exists at the Tuzla Peninsula site of the Geophysical Observatory of the North Anatolian Fault (GONAF), southeastern Istanbul, Turkey (Fig. 1). The GONAF-Tuzla array includes five levels of borehole seismometers extending down to ∼300 m depth (Fig. 2). It was the first of seven GONAF vertical arrays to be installed around the eastern Sea of Marmara (Prevedel *et al.*, 2015). The seismic data collected at Tuzla provide a base for a better

*Also at Free University Berlin, Department of Earth Sciences, Malteser Strasse 74-100, 12249 Berlin, Germany.

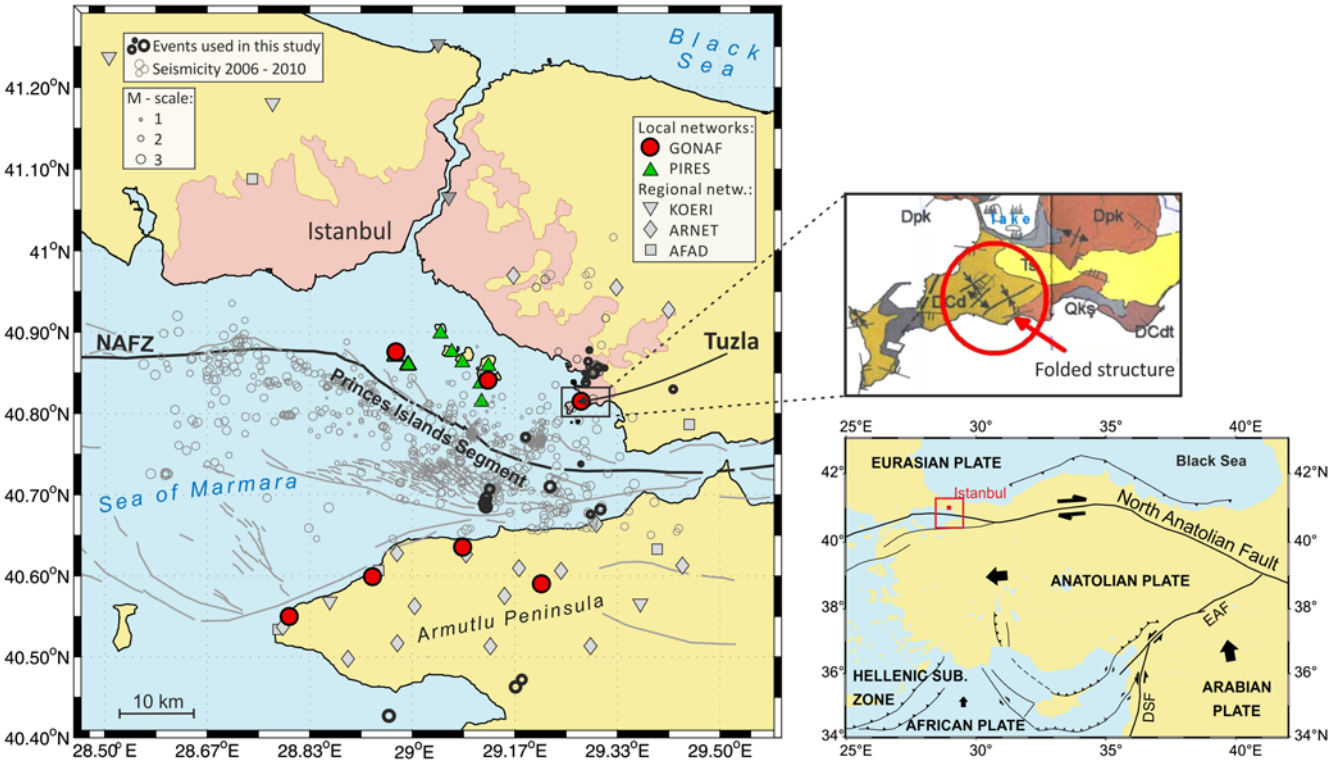

Figure 1. (Right, bottom) Location map of the Anatolian region with the main tectonic features forming the North Anatolian fault. The box marks the study area (enlarged on the left). Bold black arrows indicate the direction of plate motion with respect to stable Eurasia. (Left) Map of the eastern Sea of Marmara showing the local microseismic activity (light gray circles, after Bohnhoff *et al.*, 2013) obtained from the island-based PIRES network and selected regional seismometer stations during 2006–2010. The Geophysical Observatory of the North Anatolian Fault (GONAF) wells with vertical seismometer arrays are indicated by bold filled circles. Black open circles are the earthquakes used in this study. Fault locations are from Armijo *et al.* (2005). The bold black line marks the Princes Islands segment and adjacent portions as the main branch of the North Anatolian fault zone (NAFZ) below the eastern Sea of Marmara. (Right, top) Geological map showing the vicinity of the Tuzla area as the location of the GONAF borehole array (E. Apart, personal comm. and report, 2012). The color version of this figure is available only in the electronic edition.

understanding of wave propagation in the shallow geologic layers around this site and improve the source parameter and ground-motion estimates that are necessary for preparing hazard scenarios locally and in the immediate surrounding area of Istanbul, with its 15 million inhabitants.

We focus here on the 1-kHz-sampling-rate seismograms of 26 nearby microearthquakes recorded at Tuzla (Table 1). Our study is an initial investigation of this site's amplification, attenuation (quality factor Q), seismic velocity, and shallow wave-propagation effects. Spectral ratio techniques are widely used to determine near-surface amplification and Q (e.g., Malin *et al.*, 1988; Şafak, 1997; Assimaki *et al.*, 2008). However, as discussed later in this article, the high seismic velocities and heterogeneities at the Tuzla site lead to strong interference effects between upgoing and downgoing waves, the latter ones being reflected at the surface and at reflectors between the borehole seismometers. These interference effects cause complicated spectra, which makes a stable determination of Q based on spectral ratios difficult (Trampert *et al.*, 1993; Bethmann *et al.*, 2012). As a result, our application of them failed to give meaningful results.

Accordingly, we chose to apply an alternative approach based on deconvolution interferometry, which makes use of the complete wavefield and takes advantage of the surface reflected wave instead of regarding it as a troublesome source of interference. The method also enables us to determine the velocity structure between the borehole seismometers and to evaluate amplification and shallow wave-propagation effects.

Deconvolution interferometry is used to estimate the impulse response between two receivers (e.g., Vasconcelos and Snieder, 2008a). It is applied, for example, for imaging purposes (Vasconcelos and Snieder, 2008b), retrieving building response to ground shaking (Snieder and Şafak, 2006; Bindi *et al.*, 2015), and for determining near-surface velocities (van Vossen *et al.*, 2004; Parolai *et al.*, 2009; Nakata and Snieder, 2012). Deconvolution interferometry has also found applications in estimating site-specific Q values. Parolai *et al.* (2010) determined site-related Q values by fitting the amplitude spectrum of the deconvolved wavefield using analytical models, and Parolai *et al.* (2012) derived Q by performing a full inversion of the spectrum.

Time-domain approaches for the estimation of Q are less common. For example, Snieder and Şafak (2006) determined Q_S in a building by fitting the slopes of the logarithm of envelopes of deconvolved seismograms. Trampert *et al.* (1993) estimated Q_S between a 500-m-deep borehole

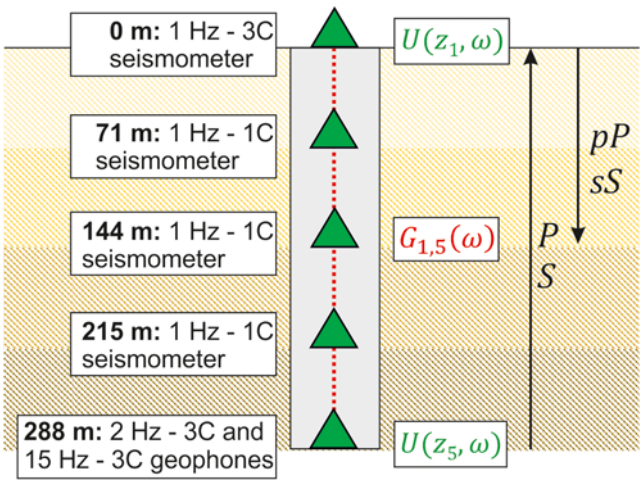

Figure 2. Sketch of the GONAF-Tuzla vertical borehole array and experiment geometry. Instruments are indicated with triangles, and the direct *P* and *S* waves (*P*, *S*) and their corresponding surface reflections (*pP*, *sS*) are sketched with arrows. Details of the instrumentation are described in Prevedel *et al.* (2015). The color version of this figure is available only in the electronic edition.

geophone and a surface seismometer by a time domain *SH*-propagator inversion. The theory of the propagator inversion technique was extended by Mehta *et al.* (2007) for the *P–SV* case for attenuating media. However, their paper did not provide an application of it to actually determine Q values.

In our data analysis, we pairwise deconvolve the downhole recordings of the 26 events with their surface recordings. The deconvolution was also checked in the reverse sense, using the deepest sensor as reference. Instead of performing an inversion as proposed by Trampert *et al.* (1993) or analyzing the deconvolved wavefield in the frequency domain as proposed by Parolai *et al.* (2010, 2012), we forward modeled the deconvolved seismograms in the time domain. With a grid search we found the seismic velocities for the *P* and *S* waves, V_P and V_S, and quality factors Q_P and Q_S that best fit the data in a least-squares sense.

For the estimation of effective velocities and quality factors, we assumed a single homogeneous layer above each borehole sensor. With the further assumption that the *P*- and *S*-wave parameters can be determined independently, the modeling procedure could be reduced to a simple 2D grid search. Given that the interferometric results and logging data reveal the presence of a low-velocity layer, these strong heterogeneities bias our Q estimates. The resulting Q values need to be regarded as apparent values that are mixtures of intrinsic and scattered attenuation and impedance effects.

Tectonic Setting and the GONAF Project

The North Anatolian fault zone (NAFZ) is a right-lateral strike-slip transform fault. It spans ~1300 km from eastern Anatolia to the northern Aegean Sea (e.g., Barka, 1992). It forms the plate boundary between the Anatolian plate in the south and the Eurasian plate in the north and slips at a rate of 20–30 mm/yr (McClusky *et al.*, 2000). This kinematic framework is driven by the northward-pushing Arabian plate in the east and the southward-pulling rollback of the Hellenic subduction zone in the west (Flerit *et al.*, 2004; Bohnhoff *et al.*, 2005) (Fig. 1, right, bottom).

In the last century, ~900 km of the NAFZ ruptured in a series of $M > 6.7$ earthquakes that started in 1939 near Erzincan in eastern Anatolia. This series then systematically propagated westward toward the Istanbul–Marmara area (Stein *et al.*, 1997). The most recent events occurred near İzmit and Düzce in 1999, which suffered M_w 7.4 and 7.1 earthquakes, respectively (Tibi *et al.*, 2001; Barka *et al.*, 2002).

The only NAFZ segment that has not experienced a major earthquake since 1766 lies to the west of the İzmit rupture and below the Sea of Marmara. It is considered to be in the final stage of its seismic cycle, with a 35%–70% probability for an $M > 7$ earthquake to occur by 2034 (Hubert-Ferrari *et al.*, 2000; Parsons, 2004). The eastern part of this Marmara seismic gap is located within 20 km of Istanbul's historic city center. Because of this regional seismic hazard and its associated risks, numerous local and regional seismic monitoring projects are being conducted along the seismic gap. One focus of these studies is the eastern part of the Marmara region offshore Istanbul.

For example, Bohnhoff *et al.* (2013) studied microearthquakes recorded by a near-fault seismic network on the Princes Islands, the PIRES network (Bulut *et al.*, 2009, 2011). Based on a 4 yr hypocenter catalog, these authors identified a ≥30-km-long aseismic fault patch extending down to 10 km depth south of the Princes Islands. They concluded that this subsegment might be locked and thus represents a potential nucleation point for an impending Marmara earthquake. This view is also supported by Global Positioning System data (Ergintav *et al.*, 2014).

The recently implemented GONAF borehole observatory is part of an intensified monitoring effort in the eastern Marmara region. It includes seven vertical arrays of seismometers in ~300-m-deep boreholes. Five of these are onland and two are on island sites surrounding the eastern Sea of Marmara (Fig. 1, left). These stations are unique in that they make use of the only possible long-term onland and near-fault sites surrounding the seismicity gap. Their borehole designs enable monitoring under low-noise conditions even in this highly populated area. As a consequence, the GONAF network has lowered the magnitude of completeness in the study area by two magnitude units with respect to the present regional networks, allowing the detection of nearly two orders of magnitude more seismic events (Prevedel *et al.*, 2015).

In this study, we use recordings from the first GONAF borehole, completed in January 2013 on the Tuzla peninsula southeast of Istanbul (Fig. 1, left). The GONAF-Tuzla array consists of a three-component (3C) Mark Products L4 seismometer with a natural frequency of 1 Hz at the surface, three L4 vertical component (1C) seismometers at ~75 m depth spacing and a bottom sonde with two 3C Geospace geophones of 2 and 15 Hz natural frequency, both in the

Table 1
Source Parameters of the 26 Earthquakes Used for Shallow Wave-Propagation Study

Event	Date (yyyy/mm/dd) Time (UTC) (hh:mm:ss.s)	Longitude (°)	Latitude (°)	Depth (km)	Magnitude (M_D)	Hypocentral Distance (km)
1	2013/05/01 17:43:50.8	29.1680	40.4630	8.2	2.7	41.0
2	2013/05/01 22:43:46.5	29.3020	40.8570	7.8	1.8	9.4
3	2013/05/01 23:13:51.9	29.2940	40.8500	7.3	2.6	8.4
4	2013/05/03 00:36:10.2	29.184	40.771	8.5	2.0	12.4
5	2013/05/03 12:17:23.1	29.282	40.842	7.2	1.1	7.8
6	2013/05/03 09:45:10.7	29.424	40.83	0.4	1.7	12.7
7	2013/05/05 20:34:24.0	29.313	40.856	5.0	-	7.5
8	2013/05/07 09:41:39.8	29.286	40.864	4.6	1.7	7.2
9	2013/05/09 04:53:04.5	29.12	40.685	8.6	2.7	21.3
10	2013/05/09 05:37:09.4	29.126	40.707	11.0	2.2	20.5
11	2013/05/09 06:05:48.5	29.117	40.689	11.6	2.5	22.5
12	2013/05/10 01:59:14.9	29.119	40.691	9.9	1.9	21.5
13	2013/05/10 08:24:42.1	29.119	40.691	9.1	2.4	21.1
14	2013/05/10 23:57:18.9	29.12	40.686	8.7	2.4	21.2
15	2013/05/11 09:52:07.8	29.28	40.85	6.0	0.9	7.2
16	2013/05/12 04:32:39.4	29.118	40.685	7.8	2.4	21.1
17	2013/05/12 23:16:13.6	29.29	40.676	7.2	1.7	17.1
18	2013/05/12 23:43:35.1	29.306	40.682	9.0	2.4	17.5
19	2013/05/14 14:26:49.5	29.288	40.878	0.6	1.2	7.1
20	2013/05/18 20:02:27.1	29.286	40.857	5.6	0.6	7.3
21	2013/05/19 19:42:21.3	29.178	40.472	7.7	2.3	39.8
22	2013/05/19 22:16:41.0	29.12	40.696	11.4	2.5	21.8
23	2013/05/21 10:05:23.3	28.962	40.427	0.0	2.9	50.6
24	2013/05/24 20:24:40.9	29.274	40.738	8.0	-	11.7
25	2013/05/26 00:11:45.8	29.224	40.71	9.1	2.6	15.4
26	2013/05/30 07:49:52.7	29.282	40.838	7.9	1.9	8.3

same housing at 288 m depth (Fig. 2). More detailed information about the borehole construction and instrumentation is given in Prevedel *et al.* (2015). In the current study, we use data from May 2013. Up to mid-May 2013 the sampling rate was 2000 Hz. It was reduced to 1000 Hz thereafter.

Local Geology at Tuzla

The Tuzla peninsula was selected for a GONAF site due to its short distance to the Princes Islands seismic gap and a prominent seismicity cluster. It also has the advantage of being at some distance from the central-city-induced seismic noise. It is, however, still within a densely populated area that includes industrial infrastructure. The groundwater level is shallow in this area, at ~10 m depth. Drilling at this site was conducted in late 2012, during which cutting samples were taken every meter.

From the cuttings, it appears that the 288-m-deep Tuzla borehole was drilled into a single limestone formation (Esen Arpat, personal comm. and report, 2012). The cuttings have the lithological characteristics of the Tuzla Limestone, a member of the Denizli Köyü formation of late Devonian age. The thickness of the Tuzla Limestone at neighboring Marmara coastal sites is estimated to be ~60 m (Özgül, 2012). However, northeast–southwest-trending tight folds have been mapped in the eastern Istanbul area (Fig. 1, right, top), which makes it difficult to obtain a reliable thickness (Özgül, 2012). There is no information available on the inclination of the beddings, but it is possible that the substantial difference between the 288 m thickness obtained from the Tuzla cuttings and the 60 m estimated from outcrops can be explained by a steeply dipping limb of folded limestone beds. This is illustrated in a simplified sketch in Figure 3a. Because of the lack of geologic cross sections from the Tuzla area, the sketches in Figure 3 are speculative but are shown here to guide our interpretation of Tuzla data.

Additional information on the local structure comes from well-logging measurements down to a depth of 258 m (Jochem Kueck, GFZ report, personal comm., 2012). The *P*- and *S*-wave velocity profiles from the sonic log are displayed in Figure 4. The sampling of these logs is 10 cm, which is substantially finer than the spatial resolution to be obtained from microearthquake waveform data, suggesting these data need to be averaged. Silva and Stovas (2009) quantified to what extent different well-log averaging methods preserve lower-frequency seismic properties and how they are suitable for velocity model building. Following their results, we generated the velocity model from the sonic log using equation (1) for calculating interval velocities:

$$V_i = \left[\left(\sum_{n=1}^{N} V(n)\right) / \left(\sum_{n=1}^{N} V(n)^{-1}\right)\right]^{-1/2}, \qquad (1)$$

in which N is the number of sonic-log velocity samples $V(n)$ within a given layer. We chose our layer boundaries to be at the sensor depths of 71, 144, and 215 m. The derived velocity model is presented in Figure 4 and listed in Table 2.

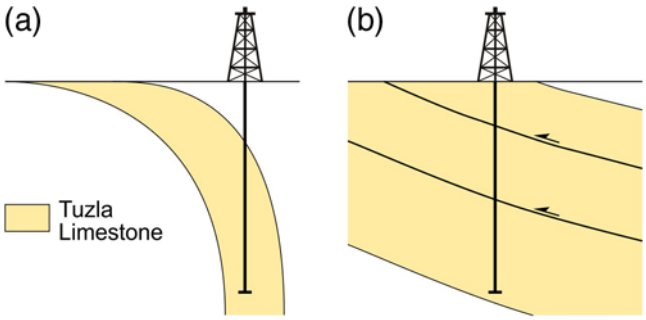

Figure 3. Sketch to illustrate two possible models derived for the observed 288-m-deep Tuzla Limestone formation. (a) The borehole was drilled into a steeply dipping limb of folded limestone beds. (b) The borehole was drilled into a repeating sequence of the Tuzla Limestone caused by thrust faulting. The color version of this figure is available only in the electronic edition.

Spectra of well-log sequences usually follow a power-law scaling of $k^{-\alpha}$, with spatial frequency k and $\alpha \approx 1$. This rule is irrespective of rock type or observation scale (e.g., Shiomi *et al.*, 1997; Leary and Al-Kindy, 2002). The α value of the Tuzla *P*-wave log is 1.01, a typical value for fractured rock, whereas the value for the *S*-wave log is 0.28. This suggests that, although the V_P log is a valid measure of the local *P*-wave velocity, the V_S log appears to be unreliable, perhaps due to some aspect of the logging procedure or well conditions.

The *P*-wave sonic log shows a complex seismic velocity structure. Most significantly, near-surface *P*-wave velocities of ~3600 m/s lie above a velocity inversion to less than ~3400 m/s at ~90 m depth. This ~50 m thick interval is followed by an increasing trend to ~4100 m/s at the bottom of the well log at 258 m.

This *P*-wave sonic log seems somewhat at odds with the uniform lithological character of the well cuttings. However, some features of the other types of well logs also indicate a more heterogeneous layering (see Ⓔ Fig. S1, available in the electronic supplement to this article). We observe relatively low resistivity values for the interval of ~85 to ~105 m and irregularities in the hole diameter caliper log at ~90 to ~140 m depth. Although these irregularities are not enough to account for the observed low velocities, they do add to their uncertainties. The resistivity and caliper logs might be interpreted as an indication for a weak zone, perhaps of thrust-faulting origin. Thus, another possible explanation for the unexpected thickness of the limestone layer could be repetition of the sequence as a result of thrust faulting associated with the local folding (Esen Arpat, personal comm., 2015) (Fig. 3b).

Dataset

We used both GONAF-Tuzla (vertical array) and PIRES (island-based surface stations) waveform recordings to compile a local hypocenter catalog to study near-surface wave-propagation effects. For earthquake detection, we applied a short-term average/long-term average trigger to the vertical-component signals from all of these stations. A seismic event was declared when three or more verticals triggered within a time window of 5 s.

We also took into account events that were too weak to be detected on the surface PIRES stations but were detected

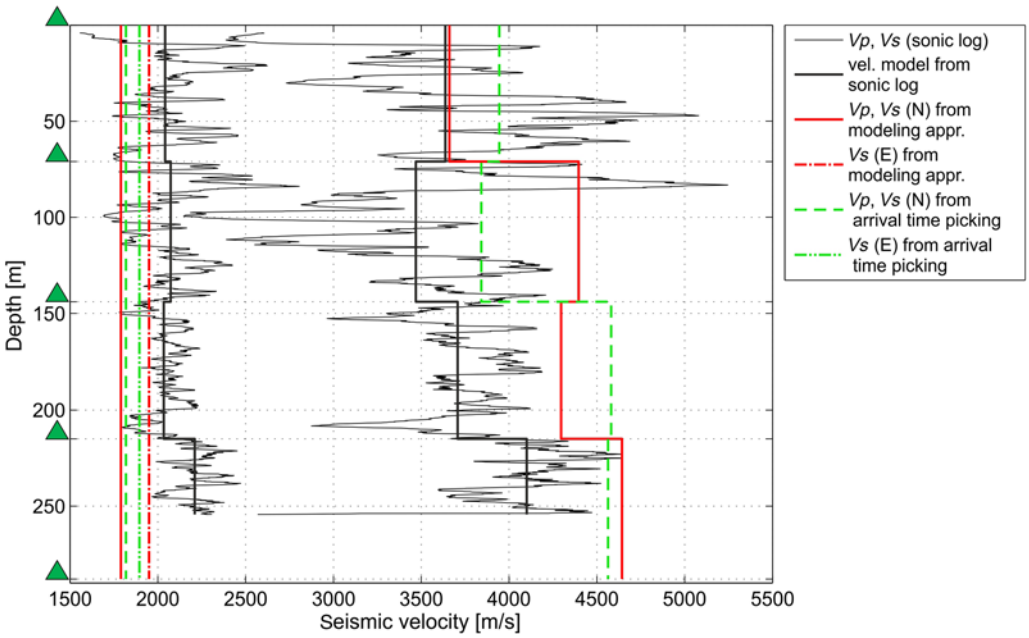

Figure 4. Sonic-log velocities (black thin line) and *P*- and *S*-wave velocity model derived from the sonic log (black bold line) are presented together with the velocity models obtained from the modeling approach and from arrival-time picking in the deconvolved seismograms. For the *S*-wave velocity, different results are obtained from the east (E) and north (N) components, thus both values are shown. Triangles on the left indicate the positions of the borehole geophones along the well (see Fig. 2). The color version of this figure is available only in the electronic edition.

Table 2
Seismic Interval Velocities between the Sensors of the GONAF-Tuzla Array Derived from Sonic Logs and Arrival-Time Picking

	Sonic Log		Arrival-Time Picking	
Depth (m)	V_P (m/s)	V_S (m/s)	V_P (m/s)	V_S (m/s) (North/East)
0–71	3637	2042	3944 ± 46	1818 ± 3/1895 ± 3
71–144	3469	2073	3842 ± 40	
144–215	3707	2034	4581 ± 63	
215–288	4100	2210	4563 ± 13	

Velocities are derived from sonic-log measurements using equation (1) and from arrival-time picking of the direct *P* and *S* waves in the deconvolved seismograms with the downhole sensor at 288 m depth used as reference (Fig. 7a,b, bottom left).

with the GONAF-Tuzla borehole array. In the May 2013 time period considered here, 188 events were detected by the combined network. Of these, 153 could be located using the HYPOCENTER computer code (Lienert *et al.*, 1986) and the optimized 1D velocity model for the eastern Marmara region of Bulut *et al.* (2007).

For this study, we selected events with signal-to-noise ratios greater than 4 at the GONAF-Tuzla sensor at 215 m depth. The ratio was calculated by dividing the root mean square amplitude of the first 0.3 s of the *P* wavetrain by that of a 10 s noise window before the *P*-wave arrival. A total of 26 events with duration magnitudes from 0.6 to 2.9 and hypocentral distances from 7 to 51 km from the GONAF-Tuzla array fit this criterion (black open circles in Fig. 1 and list of earthquakes in Table 1). The seismograms from all the 1 and 2 Hz sensors for these events were used to analyze the wave-propagation effects in the shallowest layers.

Figure 5 shows an unfiltered, but instrument corrected, waveform example from the GONAF-Tuzla array for event number 18 in Table 1. The upgoing direct *P* and *S* waves and their corresponding downgoing surface reflections (*pP* and *sS*) can be clearly seen in these seismograms. As expected, the attenuation of the waves as they travel to the surface and then down again significantly reduces their amplitudes. At the surface station, one also sees reverberations following the direct *P* wave. As we will discuss, these secondary arrivals are observed for many events and appear to be due to the shallow subsurface structure.

Method

One aim of the GONAF effort is to determine the *P*- and *S*-wave velocity and attenuation structure for each borehole site. A common method used to find the quality factor Q is the spectral ratio technique (e.g., Gibbs *et al.*, 1994; Parolai *et al.*, 2007; Ge *et al.*, 2009). It typically begins by computing the ratio of the Fourier spectra of isolated *P* and *S* waves between the surface and downhole seismograms, after taking into account instrument responses and other gain factors not related to attenuation. At the Tuzla site, the travel-time differences between *P* and *pP* and between *S* and *sS* at the 288-m-deep sensor are only ~0.13 and ~0.32 s, respectively. These separations are relatively short compared with other studies (e.g., Blakeslee and Malin, 1991; Bethmann *et al.*, 2012). This limits the bandwidth over which the spectral ratios can be fit with a constant Q model, $Q = -\pi\delta t m^{-1}$, in which m is the slope of the ratio and δt is the travel-time difference between the recording levels (Aki and Richards, 2002). These and other interference effects result in meaningless Q values.

To make use of the complete wavefield, including the signals from downgoing waves, we chose instead to apply a seismic interferometry approach to determine the characteristics of the Tuzla site. This approach also allowed us to determine the velocity structure between the borehole sensors. Several algorithms exist for interferometry, but here we focus on the deconvolution technique (e.g., Trampert *et al.*, 1993; van Vossen *et al.*, 2004; Mehta *et al.*, 2007; Parolai *et al.*, 2009; Nakata and Snieder, 2012).

We first applied instrument response corrections to each seismogram, assuming near-vertical incidence at the bottom sensor and that all sensors in the borehole are subject to the same source and path effects (from the source to the deepest sensor). The deconvolution of the earthquake signal at the sensor at depth z_1 with that at depth z_2 yields the plane-wave Green's function $G_{1,2}$ for propagation from z_2 to z_1. This can be written in the frequency domain as

$$G_{1,2}(\omega) = \frac{U(z_1,\omega)}{U(z_2,\omega)}, \tag{2}$$

in which ω is the angular frequency and $U(\omega)$ is the Fourier spectrum of the seismogram. The fraction in equation (2) also can be turned around to yield the Green's function for propagation from z_1 to z_2.

Because the signals are bandlimited, contaminated by background noise, and contain site-related notches in their spectra, the spectral division in equation (2) is inherently unstable. To prevent this instability, a regularized deconvolution is typically used. We tested two different regularizations. The first is used, for example, by Mehta *et al.* (2007), Parolai *et al.* (2009), and Nakata and Snieder (2012), and the second is the method of Helmberger and Wiggins (1971) and Dey-Sarkar and Wiggins (1976). The first turned out to be more stable for our data and is given by

$$G_{1,2}(\omega) \approx W(\omega)\frac{U(z_1,\omega)}{U(z_2,\omega)}, \tag{3}$$

in which

$$W(\omega) = \frac{|\mathrm{U}(z_2,\omega)|^2}{|U(z_2,\omega)|^2 + \varepsilon} \tag{4}$$

is the filter; hence,

$$G_{1,2}(\omega) \approx \frac{U(z_1,\omega)U(z_2,\omega)^*}{|U(z_2,\omega)|^2 + \varepsilon}. \tag{5}$$

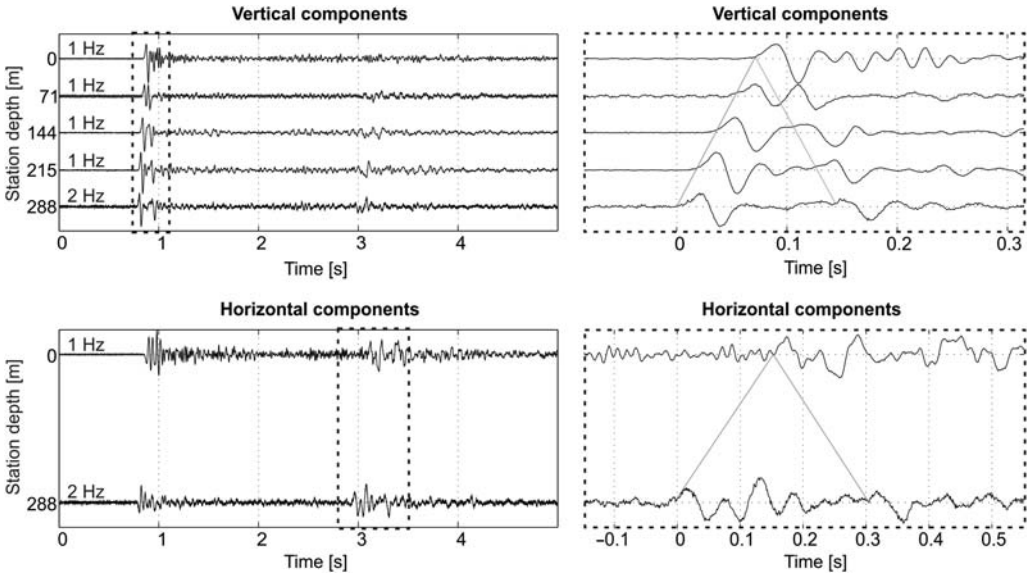

Figure 5. Waveform example from vertical and north–south horizontal components of the GONAF-Tuzla array. The respective sensor depth is plotted at the *y* axis, and each trace is normalized to its maximum. The instrument response has been corrected, and the seismograms are otherwise unfiltered. Only the surface station and the very deepest sensor have horizontal components. (Left) Complete waveforms of event 18 (Table 1), and (right) close-up windows of the same event containing only the (top) *P* wave and (bottom) *S* wave, respectively. The direct upgoing *P* and *S* waves and their corresponding downgoing surface reflections are marked with gray lines.

The regularization parameter ε refers to a constant added to the denominator to prevent numerical instabilities in equation (2) (e.g., Parolai *et al.*, 2009). It is chosen as a percentage of the average spectral power of $U(\omega)$ at the station selected as reference. Tests have shown that an ε of 3% seems to be the appropriate value for our data.

Data Processing

To use the horizontal components of the surface and downhole sensors, it is necessary to rotate the downhole horizontal components into the north and east directions so that their orientation equals the orientation of the surface horizontal components. How the rotation angle is determined is explained in detail in the Appendix.

After orienting the downhole horizontal components, the seismograms of all channels were then rotated into radial and transverse directions and corrected for instrument response and direct current offset. As in previous deconvolution studies (Mehta *et al.*, 2007; Parolai *et al.*, 2009), our results were insensitive to the data window selection. Accordingly, we chose to use windows containing the complete signal of the event. This data window was tapered to avoid spectral leakage.

The deconvolution was performed by applying equation (5). The bandwidth of the deconvolution was set to 0.1–40 Hz, as all 26 events have energy at least up to ~40 Hz (see spectra in Ⓔ Figs. S2–S14). The lower limit of the bandpass turned out to be helpful in removing very-low-frequency noise, but its influence on the deconvolution result was only minor. Thus, a low corner frequency of 0.1 Hz was chosen to include as many octaves of bandwidth as possible. As the last step, all the deconvolved spectra are inverse Fourier transformed into the time domain and then stacked to improve the signal-to-noise ratio. The stacking requires the assumption of nearly vertical incidence, meaning equal moveouts along the borehole for all events. We checked these times in the deconvolved seismograms and found only minor traveltime differences of <0.01 s. Figure 6 shows the surface-to-144 m vertical-component deconvolution results for each event and their stacking result.

Deconvolution Results and Discussion

Figure 7a,b displays the deconvolved seismograms with the surface and 288 m sensor used as reference. When the signal at the surface is used as the reference, the upgoing waves are mapped onto times before their surface arrival. Thus, the upgoing and downgoing waves are symmetric around the surface arrival time, which is taken to be the zero reference. When the 288 m sensor is used as the reference, all the signals appear after its arrival time. In Figure 7a, each trace is normalized to its maximum to show the relatively small downgoing signal amplitudes at the deepest sensor. To allow for amplitude comparisons between different depth levels, each trace in Figure 7b is normalized to the maximum of the entire array.

Figure 7b shows clearly how the amplitude of the upgoing wave decreases while propagating from 288 to 71 m depth. However, in the upper tens of meters between the sensor at 71 m depth and the surface, the amplitude increases. After correcting for the free-surface amplitude factor of 2, the surface sensor still records a 1.7 times stronger signal than the sensor at 71 m. This factor of 2 is only correct for vertically incident and *SH* waves. For *P* and *SV* waves, it varies with incidence angle and can be even below 1 (Shearer and Orcutt, 1987). The am-

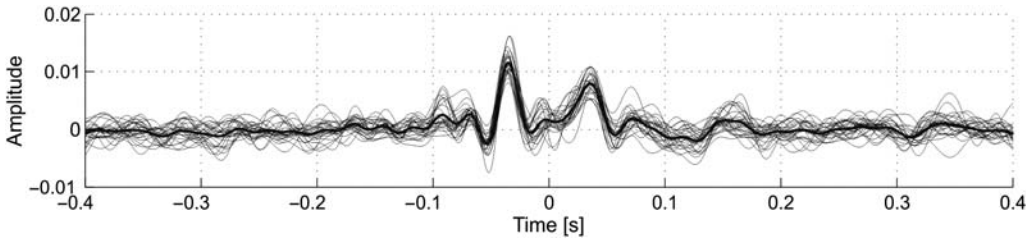

Figure 6. Seismograms from the sensor at 144 m depth after deconvolution from the surface signal. Thin traces show the results from each of the 26 events. The bold trace is the stacked deconvolved seismogram.

plitude increase in the upper few tens of meters indicates that, in these shallow depths at the Tuzla site, amplification due to impedance contrasts influences the waveforms more strongly than the effects of attenuation. If these impedance effects are not taken into account, it is only possible to determine an apparent attenuation, as will be discussed later.

The average seismic velocities between sensors can be calculated from the travel-time differences between them in the deconvolved records (Table 2 and Fig. 4). Because only the surface sensor and the sensors at 288 m depth have horizontal components, an average *S*-wave velocity could be determined only between them.

The arrival-time picking of the direct upgoing *P* wave shows that a strong change in *P*-wave velocity exists somewhere between 71 and 215 m depth (Fig. 7a,b, bottom left). Further, two reflected *P* waves can be seen in the deconvolved seismograms. These are marked with gray dashed lines in Figure 7. The upgoing reflected wave (seen on the bottom left in Fig. 7a,b) and the downgoing reflected wave (seen on the top left in Fig. 7a,b) appear to originate from an interface between the sensors at 71 and 144 m. Such a horizon could correspond to the low-velocity zone evident in the sonic-log velocity profile between ∼90 and ∼140 m depth (Fig. 4). Reassuringly, the polarities of the reflected waves agree with the presence of a low-velocity layer. The reverberations after the direct *P*-wave arrival at the surface sensor seen in the unfiltered seismograms (Fig. 5) could be created by multiple reflections from this layer.

The arrival-time picking of the *S* wave suggests that the *S*-wave velocity appears to be 4% slower on the north component than at the east component. This could be an indication of shear-wave splitting (a difference in *S*-wave velocity as a function of azimuth) rather than an artifact of the method. The eastern Sea of Marmara is known to show this type of anisotropy, as reported by Hurd and Bohnhoff (2012) and Eken *et al.* (2013). The *S* anisotropy in the depth range of ∼3 to ∼10 km was estimated to be ∼1%–3%. Moreover, Eken *et al.* (2013) also found the fast polarization direction north of the Princes Islands segment to be parallel to the main NAFZ strand and along the maximum horizontal stress direction, $S_{H\max} \sim$ N125°E (Kiratzi, 2002; Bohnhoff *et al.*, 2006). These observations could account for the splitting direction seen at Tuzla. A further indication for having a true shear-wave splitting observation in our data is that following Nakata and Snieder (2012) deconvolution interferometry can be used for shear-wave splitting analysis, which, however, would be beyond the scope of this study.

Forward Modeling

We modeled the deconvolved seismograms from the Tuzla site with the layered, frequency–wavenumber propagator method of Wang (1999). The source for these time-domain synthetic seismograms was placed 1 km directly below the receiver points. The aim was to obtain a first-order estimate of the apparent *P*- and *S*-wave *Q* values and to refine the velocities of the layers between the sensors.

Because of the uncertainties introduced by the unconstrained structures evident at the Tuzla site, we chose to reduce the layering above each sensor to a single, homogeneous, effective unit. This approach allowed us to use a grid search method for the best-fit model. It resulted in four different effective *P*-wave velocity and attenuation models, covering the depth ranges 0–71, 0–144, 0–215, and 0–288 m. The effective *S*-wave velocity and quality factor were determined for a homogeneous layer between the horizontal components at 0–288 m. These effective parameters are indicated here by an overbar, as in $\overline{V_P}$ versus V_P for the interval velocities and $\overline{Q_P}$ for the effective quality factors. We discuss later how these values relate to ones that might have been obtained for the individual intervals.

After the computation of synthetic seismograms, the same processing steps as for the observed waveform data were applied and then the results compared to the observations. In our grid search, we sought to find the minimum misfit between the observed amplitudes and arrival times of the upgoing and downgoing waves (A_u^o, A_d^o and t_u^o, t_d^o) and their corresponding synthetic values (A_u^s, A_d^s and t_u^s, t_d^s), as given by

$$m(V,Q) = \sqrt{(A_u^o - A_u^s)^2 + (A_d^o - A_d^s)^2 + (t_u^o - t_u^s)^2 + (t_d^o - t_d^s)^2}. \quad (6)$$

To reduce computation time, this 4D grid search (V_P, Q_P, V_S, and Q_S) was separated into two 2D searches, with the *P*- and *S*-wave parameters being determined independently. Q_S and V_S for *SH* waves are inherently independent of Q_P and V_P. For the *P*–*SV* case, the *S* parameters are held fixed while determining V_P and Q_P and, similarly, for Q_S and V_S. Also, under the assumption of frequency constant Q_P, V_P could be determined independently from the other

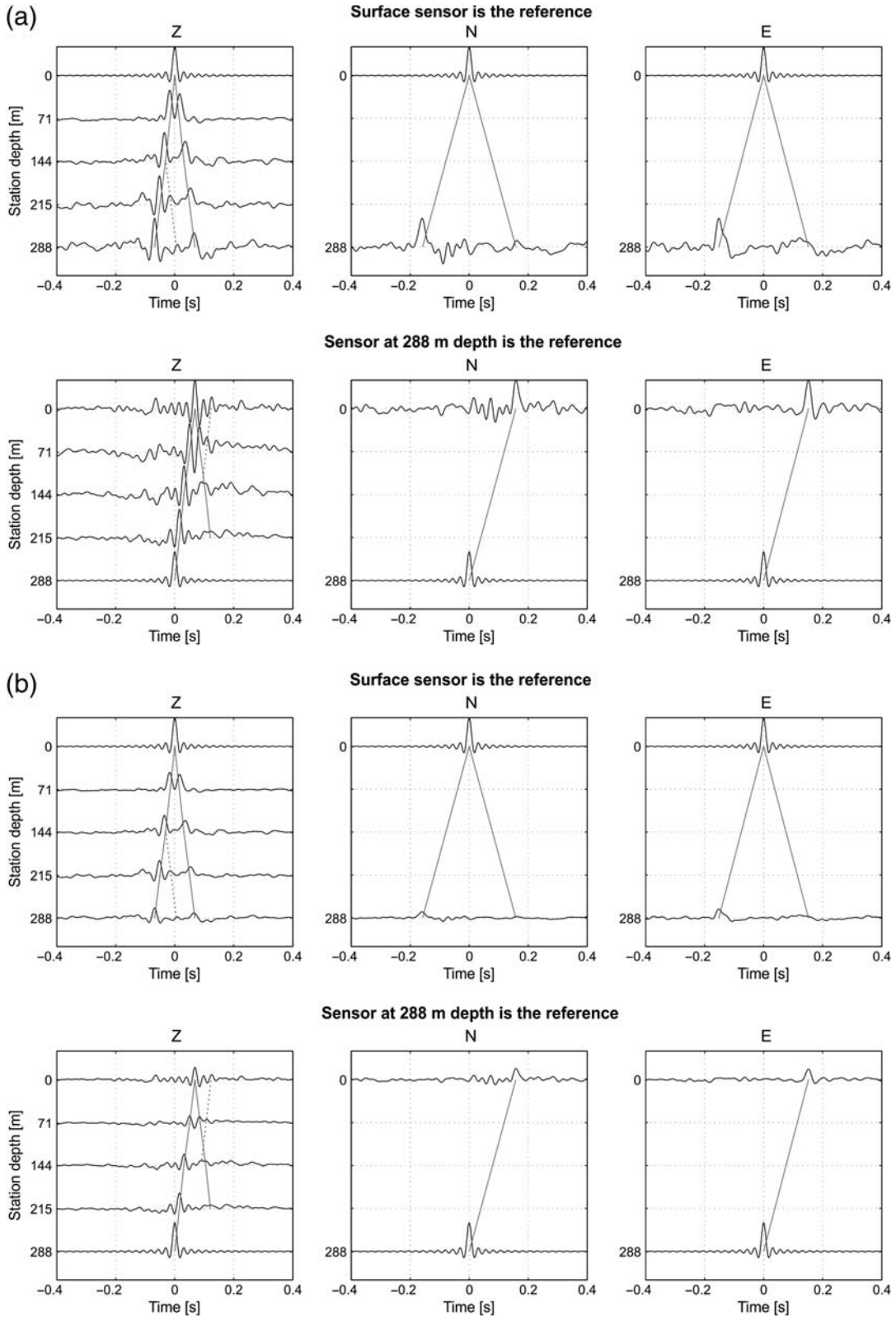

Figure 7. Stacked deconvolved seismograms from vertical and horizontal components. One time the surface sensor is used as the reference sensor (top), and the other time the sensor at 288 m depth is used as the reference (bottom). Gray solid lines mark the travel times of the direct upgoing and downgoing waves, and dashed gray lines indicate reflected phases. (a) Each trace is normalized to its maximum. (b) Each trace is normalized to the maximum of the entire array.

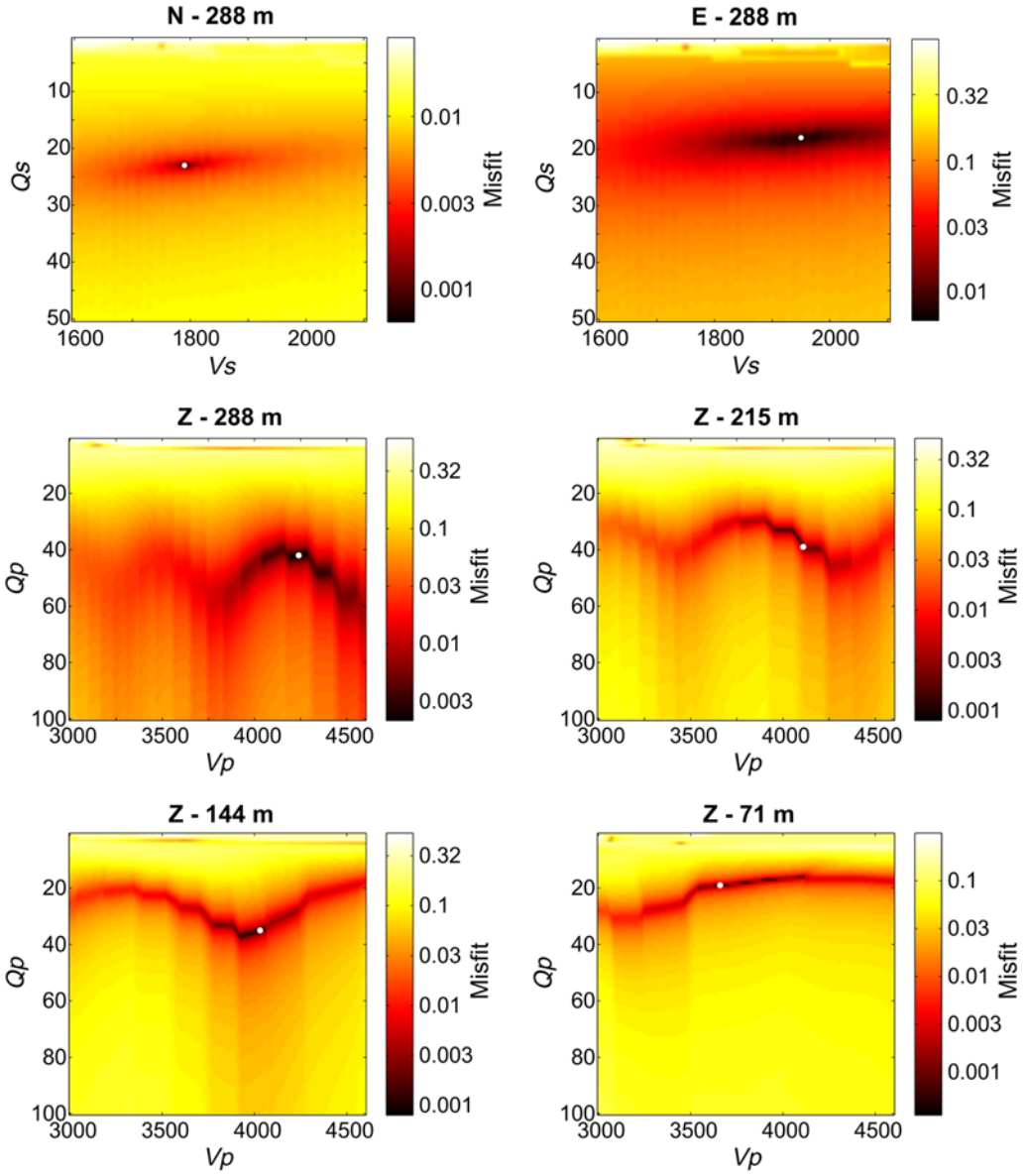

Figure 8. Misfit functions of all three components for the sensor at 288 m depth and for all verticals. The horizontal components north and east were used for the determination of V_S and Q_S and the vertical Z components for the determination of V_P and Q_P. The white dot marks the minimum of each misfit function. The color version of this figure is available only in the electronic edition.

parameters, because it depends only on the arrival times of the P wave. Only Q_P has a dependency on both, P- and S-wave velocity, because it is determined from the amplitude of the P-wave recording, which in turn depends on the impedance contrast that is controlling the amount of energy reflected and refracted as a P wave and converted S wave. Under the assumption of vertical incidence, these conversions are reliable. Nevertheless, even if this assumption is broken, if the S-wave velocity is fixed to a value close to the true value, the error in Q_P introduced by this simplification will be small, as we will show. For the P- and S-wave parameters, we searched a range of velocities from 3000 to 4600 m/s and 1600 to 2100 m/s, and quality factors from 1 to 100 and 1 to 50, respectively.

The misfit functions are presented in Figure 8, with their minima marked by a white dot. For all three components, we observe that, in the misfit functions, the apparent Q values are well constrained, whereas the velocities appear less well constrained. Nonetheless, clear minima can be observed for the horizontal components but less so for the vertical components. To better constrain the velocity, tests have shown that the terms in equation (6) containing the arrival times should be weighted more heavily than the amplitude terms. This, however, reduces the capability for resolving Q. Because we already have good velocity information from sonic-log data and arrival-time picking in the deconvolved seismograms, we decided against a velocity-weighted misfit function to obtain better constrained Q values. On the east (E) component, the

Table 3
Effective Seismic Velocities and Apparent Quality Factors Obtained from the Forward Modeling Approach

Depth (m)	$\overline{V_P}$ (m/s)	$\overline{Q_P}$	$\overline{V_S}$ (m/s) (N/E)	$\overline{Q_S}$ (N/E)	Depth (m)	V_P (m/s)	Q_P
0–71	3660	19			0–71	3660	19
0–144	4030	35			71–144	4396	160
0–215	4110	39			144–215	4296	54
0–288	4240	42	1790/1950	23/18	215–288	4643	56

The parameters marked with overbars are the effective velocities and apparent quality factors corresponding to a homogenous layer between the surface and the sensor. *S*-wave parameters could be determined for the depth range 0–288 m only, and they were derived independently on the north and east components. The parameters written without overbars correspond to a specific depth interval.

velocity and Q are less constrained compared with the north (N) component. This is because the downgoing wave is poorly resolved on the east component due to interference with two peaks that precede its arrival (Fig. 7a, top right).

The best-fit model effective velocities and quality factors are summed in Table 3. We observe increasing Q_P with increasing depth and $\overline{Q_P}(288\text{ m}) \approx 2\overline{Q_s}(288\text{ m})$, which is in good correspondence with theory. Overall, the average *P*-wave velocities obtained from the modeling approach are very similar to the *P*-wave root mean square velocities derived from the arrival-time picking. Going from the shallowest homogeneous layer to the deepest, these are 3944, 3892, 4106, and 4217 m/s. The effective *P*-wave velocities obtained from the modeling approach can be transferred to interval velocities using the Dix equation (Dix, 1955) (see Table 3). These values are in contrast to the velocities derived from arrival-time picking, and the *P*-wave sonic log: the forward modeling places a more modest low-velocity layer at a deeper depth.

Figure 9 presents the model seismograms computed with the parameters listed in Table 3 in comparison with the observed deconvolved seismograms. The modeled upgoing and downgoing *S* and *P* waves on the north and vertical (*Z*) components fit better than on the east component. This can be explained by the weak downgoing *S* wave on the east component, which interferes with two preceding signals.

Error Analysis

From Figures 8 and 9, it can be concluded that our simple forward modeling approach gives well-constrained velocities and apparent quality factors. However, the simplifications of (1) a homogeneous layer and (2) deriving *P*- and *S*-wave parameters independent from each other can introduce significant errors. To evaluate these, we computed synthetic seismograms for several models. These include one-layer models, two-layer models (with both a faster layer over a slower layer, and vice versa), and four-layer models based on the sonic logs and the velocities derived from the modeling approach and arrival-time picking. To define *S*-wave velocities for the shallower layers in the four-layer models, a V_P/V_S ratio of 2.27 [i.e., $\overline{V_P}(288\text{ m})/\overline{V_S}(288\text{ m})$] was assumed. The modeling approach results and the ones from arrival-time picking give this same V_P/V_S ratio. For each layer of the four-layer models, we use equation (2) in Tonn (1991) for the calculation of interval Q_P values from the effective values obtained from the modeling approach. The interval Q_P values are 19, 160, 54, and 56 from the shallowest to the deepest layer. The interval Q_S values are set to $Q_P/2$.

We apply to the synthetic data the same forward modeling approach as used for the recorded waveform data. While performing the grid search for V_S and Q_S, the *P*-wave velocity was fixed to 4200 m/s ($V_{P,\text{mod}}$). This is close to the root mean square velocity of a homogeneous layer above the sensor at 288 m, as determined from arrival-time picking in the deconvolved seismograms. During the grid search over V_P and Q_P, the *S*-wave velocity was fixed to 1850 m/s ($V_{S,\text{mod}}$). This is between the two *S*-wave velocities derived from arrival-time picking: 1818 and 1895 m/s on the north and east components, respectively. During the error analysis, we evaluate how the error depends on the difference between the fixed velocity (V_{mod}) and the real one (V_{real}). We call the difference between these velocities ΔV.

The error estimates from the one-layer models and the four-layer models are summarized in Table 4. As expected, the simple one-layer models yield very small errors for V_S and Q_S. Furthermore, we did not observe a dependency of the *S*-wave parameters on ΔV, which is also as expected, because they are determined from the *SH* component, which does not contain *P*-wave energy. The four-layer models also show small errors in V_S, but the errors in Q_S increased noticeably due to the unconstrained impedance contrasts between the sensor levels.

The errors in V_P for the one-layer and four-layer models are similar to the errors of V_S. It also appears that V_P is insensitive to changes in ΔV. In contrast, it is more difficult to evaluate the error in Q_P due to its strong dependency on ΔV. The range of errors in Q_P given in Table 4 is based on the assumption that $V_{S,\text{real}}$ differs from $V_{S,\text{mod}}$ by no more than $\pm 10\%$. The first table value corresponds to -10% ($V_{S,\text{real}} > V_{S,\text{mod}}$) and the second to $+10\%$ ($V_{S,\text{real}} < V_{S,\text{mod}}$). A negative error implies that Q_P is underestimated, and positive values correspond to overestimation. We observe that the modeling approach has a tendency to overestimate the *P*-wave quality factor. Keeping in mind that $V_{S,\text{mod}}$ has been chosen based on the *S*-wave velocity measured on the deepest sensor, $V_{S,\text{real}}$ at the shallower sensors is probably smaller than $V_{S,\text{mod}}$. Hence, the expected

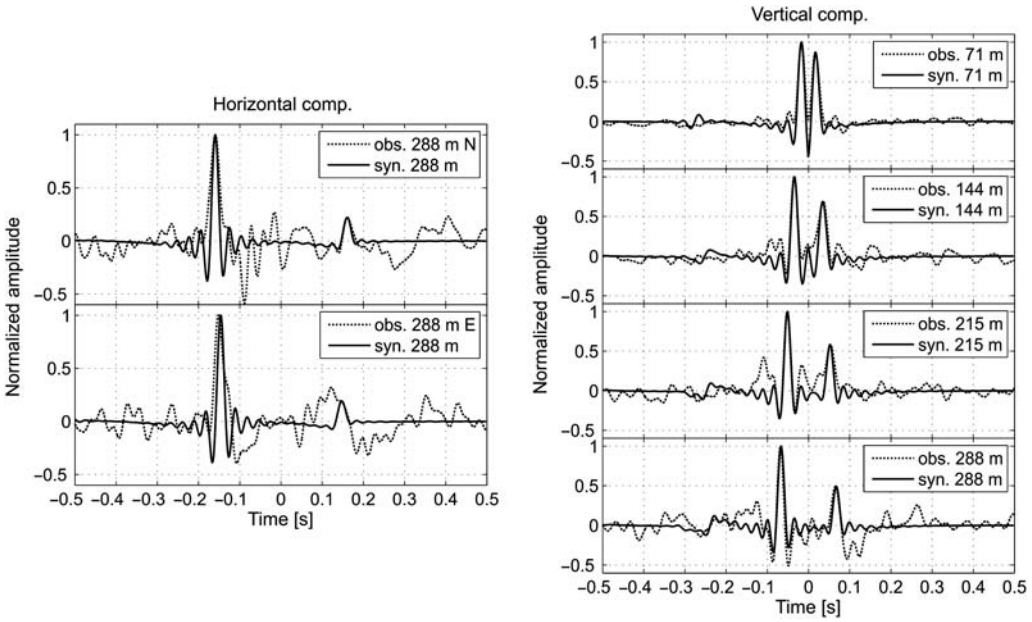

Figure 9. Comparison of waveforms of the observed (obs) and synthetic (syn) deconvolved seismograms. The solid traces show the deconvolved synthetic seismograms for the best fit (parameters are listed in Table 3). The observed deconvolved seismograms are plotted with a dotted line.

error in Q_P corresponds to $\Delta V = +10\%$ rather than the value given for -10%. Considering that $V_{S,\mathrm{mod}}$ is close to the *S*-wave velocity determined from arrival-time picking at 288 m depth, the range of $\pm 10\%$ is probably too large for the deep sensors. For the shallower sensors, this range could be realistic.

In summary, it appears that the simplification of a homogeneous layer over each sensor has only a minor effect on V_S and V_P, whereas the errors in the *P*- and *S*-wave quality factor increase with increasing model complexity. The simplification of determining V_S and Q_S independent from V_P and Q_P only affects the accuracy of Q_P.

The errors of the velocities and Q depend also on the stability of the deconvolution result of the observed data. To evaluate this, we performed a jackknife test. To do this test, we successively removed two different earthquakes from the 26 events. For each subset, the stacked deconvolved seismograms were computed, and the amplitudes and arrival times of the upgoing and downgoing waves were determined. They were then forward modeled by minimizing equation (6) to determine the velocities and quality factors. These results are presented in Figure 10 in the form of histograms, which show the distributions of V and Q. Because Q depends on the logarithm of the amplitude ratio between upgoing and downgoing waves, we observe a lognormal distribution of Q (Fig. 10, right). Hence, for Q, the logarithmic mean and standard deviation was calculated. In contrast to that, there is no specific distribution observable for V (Fig. 10, left). For V, we calculate the mean and standard deviation of a normal distributed dataset. The values of the mean and standard deviation of Q and V are given in the legends in Figure 10. These calculations show that the deconvolution results are mostly stable. However, for the sensor at 71 m depth, we observe a larger standard deviation of V_P of ~4%; and, for the sensor at 288 m depth, Q_P has a large standard deviation of ~27%.

The errors of the velocities derived from arrival-time picking in the deconvolved seismograms are determined with the same jackknife test. These are around 1% (see Table 2).

Discussion

With deconvolution interferometry, we analyzed near-surface wave-propagation effects, such as amplification and attenuation, and determined the velocity structure below the Tuzla site in southeastern Istanbul. From arrival-time picking in the deconvolved seismograms and from forward modeling the Green's functions, we derived two different velocity models down to 288 m depth. The first model sees a low-velocity zone between the sensors at 71 and 144 m and the second one between the sensors at 144 and 215 m depth (Fig. 4). Because logging measurements confirm a low-velocity zone between ~90 and ~140 m, the first velocity model seems to be more reliable. Despite these differences, both models have similar root mean square velocities. This reflects the common problem of uniqueness: several models can describe the same observation. In our modeling approach, we focused on fitting the amplitudes and travel times of the direct upgoing wave and its surface reflection. If we also would have taken into account the arrival times of the phases that are reflected from the low-velocity layer (gray dotted lines in Fig. 7a,b), we might have been able to better constrain the low-velocity zone at the right depth. However, this was not possible, because we performed a simple grid search for a homogeneous layer above each sensor. For future modeling studies, we recommend choosing more complex techniques (e.g., a full wavefield inversion) to be able

Table 4
Estimated Errors of the Results from the Modeling Approach

	One-Layer Models				Four-Layer Models			
Depth (m)	Err. $\overline{V_S}$ (%)	Err. $\overline{Q_S}$ (%)	Err. $\overline{V_P}$ (%)	Err. $\overline{Q_P}$ (%)	Err. $\overline{V_S}$ (%)	Err. $\overline{Q_S}$ (%)	Err. $\overline{V_P}$ (%)	Err. $\overline{Q_P}$ (%)
71	0.9	6.5	4.4	+100 – (−27)	3.3	20.3	5.5	+35 – (−27)
144	0.4	1	1.4	+51 – (−6)	0.7	8.8	1.2	+81 – (+3)
215	0.3	0.6	0.6	+34 – (−9)	0.5	7.9	0.7	+65 – (+7)
288	0.25	0.1	0.7	+13 – (−8)	0.5	5.1	0.7	+43 – (+7)

Summary of error analysis: The errors presented here are the average errors obtained from several one-layer models and four-layer models. The error bounds given for $\overline{Q_P}$ correspond to a range of $\Delta V = -10\% - (+10\%)$ (see explanation in the text). Positive values indicate an overestimation of $\overline{Q_P}$, and negative values an underestimation.

to better capture the heterogeneities in the subsurface. Further, additional information from logging would be invaluable.

Both of our *P*-wave velocity models derived from interferometry overestimate the *P*-wave sonic-log velocities by ~10%–20%, even though the estimated errors for the velocities are only ~1%–5%. One possible reason for an overestimation is the assumption of vertical incidence of the incoming wavefield. If this assumption is not fulfilled, apparent higher velocities will be determined. Another reason for the difference in velocities could be related to the higher frequencies used in sonic-log measurements that sample only a few decimeters around the borehole. Thus, the seismic waves sample a larger volume of the rock formations, including potential lateral variations. A comparison of our *S*-wave velocity model with the sonic-log *S*-wave velocity model is not reasonable, because the latter is likely to be erroneous, as discussed in the Local Geology at Tuzla section.

The forward modeling approach allowed us to determine apparent *P*- and *S*-wave quality factors. The apparent Q_P values for the depth ranges 0–71, 0–144, 0–215, and 0–288 m increase with depth, and we find $Q_P \approx 2Q_S$, in accordance with theory. Nevertheless, our Q estimates have to be interpreted with caution. They are biased due to the fact that we did not account for impedance changes during the modeling, because we assumed in the model a single homogeneous layer above each sensor. Thus, our apparent Q values contain both intrinsic and scattered attenuation and impedance effects. The latter means that, if waves travel from higher to lower impedance layers, as in our case between the sensors at 288–71 m, the decreasing impedance causes amplification

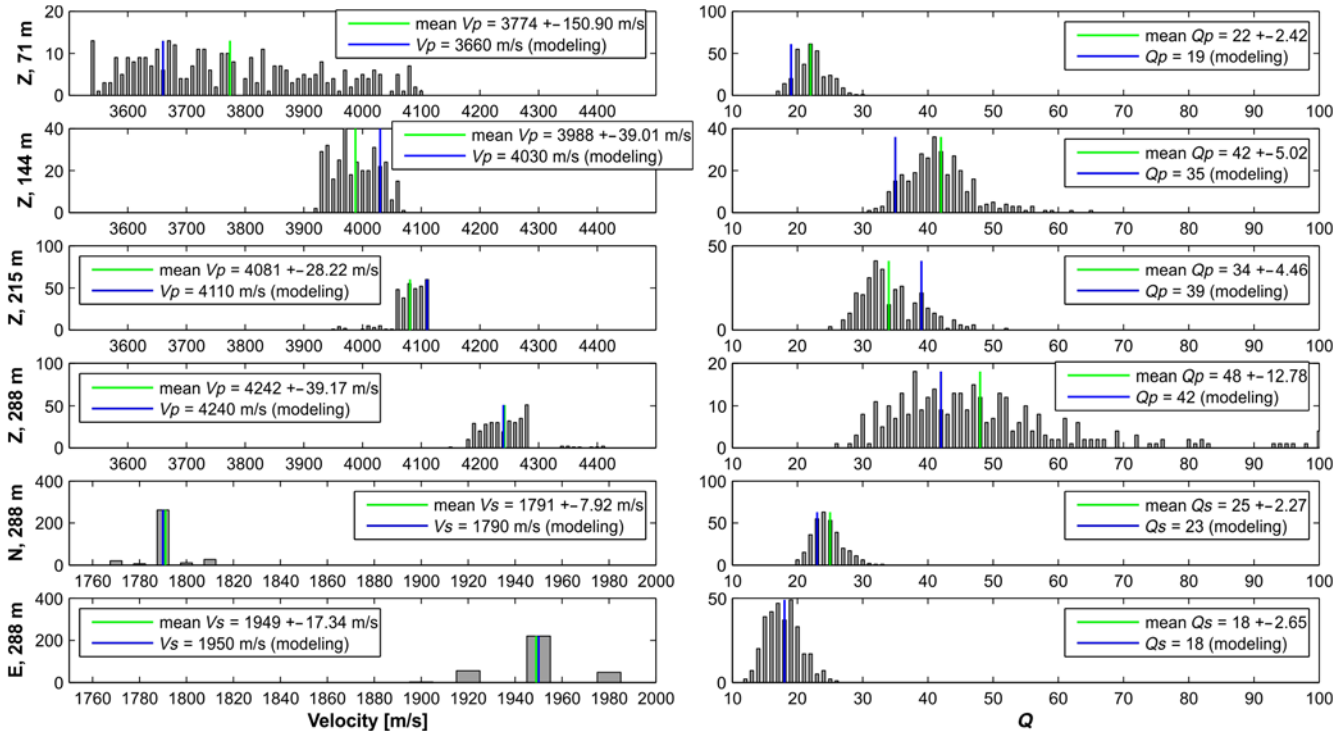

Figure 10. Results of the jackknife test. The histograms present the distribution of results obtained from each subset. (Left and right) present the results for *P*- and *S*-wave velocity and quality factors, respectively. The mean and standard deviation and results of the modeling approach are marked with lines and given in the legend. The color version of this figure is available only in the electronic edition.

due to energy conservation, with energy being proportional to ρVA^2 (ρ is density, V is velocity, and A is amplitude). This impedance amplification could lead to apparent higher Q values. On the other hand, increasing impedances, as in our case from the low-velocity zone to the layer above, would lead to apparent lower Q values. Despite this bias, which causes large errors especially in Q_P, our apparent quality factors are similar to the ones found in other studies in the Marmara Sea region. For example, Parolai *et al.* (2010) estimated Q_S values of 30, 46, and 99 for the depth ranges 0–50, 0–70, and 0–140 m in Ataköy (western Istanbul). They also used the recordings of a vertical borehole array and fitted the borehole-to-surface spectral ratios with a theoretical transfer function to derive Q_S. Using the ratio between *S*-wave and coda-wave amplitudes, Gündüz *et al.* (1998) determined a frequency-dependent average *S*-wave attenuation of $Q_s(f) = (50 \pm 1.7) f^{1.09 \pm 0.05}$ for the crust below the Sea of Marmara, which is higher than our Q_S because they sample larger depths down to the base of the crust.

Conclusions

We studied the first-order wave-propagation effects at the GONAF-Tuzla vertical array in southeastern Istanbul, Turkey. Using a seismic interferometry technique based on deconvolution and a simple forward modeling approach, we obtained estimates of near-surface apparent quality factors and seismic velocities for *P* and *S* waves.

The near-surface seismic velocities at the Tuzla site are high compared with other Istanbul sites and other borehole sites around the world with comparable depth. We found *P*-wave velocities of more than 3600 m/s and *S*-wave velocities of ~1800 m/s in a 300-m-deep borehole. An additional uniqueness comes from a strong impedance change somewhere between 71 and 215 m depth, which is probably related to a velocity inversion observed by sonic logs between ~90 and ~140 m depth. These impedance steps introduce reverberations in the recordings of the surface sensor, and the high velocities lead to strong interference of upgoing and downgoing waves on the downhole sensors.

Because of the given complicated structure and the resulting impedance contrasts, it was not possible to derive attenuation parameters with standard techniques such as spectral ratios. Instead, we proposed a forward modeling approach and found that the apparent Q_P increases with depth, with values of 19, 35, 39, and 42 for the depth ranges 0–71, 0–144, 0–215, and 0–288 m. For the apparent Q_S, we observe a value of ~20 for the depth range 0–288 m. These attenuation estimates are interpreted to be biased by the strong heterogeneities observed at the Tuzla site.

If borehole seismometers are installed within a relatively simple almost homogeneous subsurface, our forward modeling approach based on a 2D grid search would be sufficient to derive reliable quality factors. However, in the presence of a complex geologic setting, such as at the Tuzla site, it is recommendable to use more comprehensive modeling techniques that invert for Q and impedance contrasts simultaneously and also take the incidence angle into account.

Our results are derived from a carefully selected set of local microseismic events, with a bandwidth between 0.1 and 40 Hz. They were obtained from the first available data from the recently implemented GONAF observatory and are encouraging signs of this network's utility. They reveal not only the complex near-surface factors that need to be considered in ground-motion studies of the Tuzla site, but also open the door for more sophisticated analysis and modeling research.

Data and Resources

Seismograms used in this study were collected by instruments of the GONAF-Tuzla vertical array as part of the Geophysical Observatory at the North Anatolian Fault (GONAF) borehole network, jointly operated by the Helmholtz Centre Potsdam GFZ German Centre for Geosciences and the Disaster and Emergency Management Authority (AFAD; https://www.afad.gov.tr/en/Index.aspx, last accessed April 2016), Ankara, Turkey. Waveform recordings are proprietary and will be released with a retention period of three years. Data will be made available through the GEOFON webpage (http://geofon.gfz-potsdam.de, last accessed April 2016) hosted at GFZ Potsdam and through AFAD Ankara. Borehole logs were provided from the International Continental Drilling Program Operational Support Group (ICDP-OSG) and are freely available. All data processing and generation of figures was done using MATLAB (www.mathworks.com/products/matlab, last accessed April 2016) software, v.R2012a.

Acknowledgments

The Geophysical Observatory at the North Anatolian Fault (GONAF) project is funded by the Helmholtz Centre Potsdam GFZ German Centre for Geosciences; the Disaster and Emergency Management Authority (AFAD), Ankara, Turkey; the International Continental Drilling Program (ICDP); and the Helmholtz Association, Germany. We acknowledge funding within the Helmholtz Young Investigators Group "From Microseismicity to Large Earthquakes" and from the German Research Foundation (DFG) within the project Bo1877/7. The GONAF instrumentation was assembled by the technical staff of the Institute of Earth Science and Engineering (IESE). We thank Georg Dresen and Murat Nurlu for their strong and invaluable support in the GONAF project. Fatih Bulut was onsite party chief and, together with Recai Kartal, managed to improve local recording conditions at the Tuzla site, which is highly appreciated. We thank the ICDP Operational Support Group, in particular Jochem Kueck, for conducting the logging measurements and Bütün Geothermal Ltd. for performing the drilling of the Tuzla well. We also would like to thank Esen Arpat from the Technical University of Istanbul for the Tuzla borehole-cutting analysis and his valuable contribution to understanding the geology at Tuzla.

References

Abercrombie, R., and P. Leary (1993). Source parameters of small earthquakes recorded at 2.5 km depth, Cajon Pass, southern California: Implications for earthquake scaling, *Geophys. Res. Lett.* **20,** 1511–1514.

Aki, K., and P. G. Richards (2002). *Quantitative Seismology: Theory and Methods*, Second Ed., W. H. Freeman and Company, New York, New York.

Armijo, R., N. Pondard, B. Meyer, G. Uçarkus, B. M. de Lépinay, J. Malavieille, S. Dominguez, M.-A. Gustcher, S. Schmidt, C. Beck, *et al.* (2005). Submarine fault scarps in the Sea of Marmara pull-apart (North Anatolian fault): Implications for seismic hazard in Istanbul, *Geochem. Geophys.* **6,** Q06009, doi: 10.1029/2004GC000896.

Assimaki, D., W. Li, J. H. Steidl, and K. Tsuda (2008). Site amplification and attenuation via downhole array seismogram inversion: A comparative study of the 2003 Miyagi-Oki aftershock sequence, *Bull. Seismol. Soc. Am.* **98,** 301–330.

Barka, A. A. (1992). The North Anatolian fault zone, *Ann. Tetonicae* **6,** 164–195.

Barka, A., H. S. Akyüz, E. Altunel, G. Sunal, Z. Çakir, A. Dikbas, B. Yerli, R. Armijo, B. Meyer, J. B. de Chabalier, *et al.* (2002). The surface rupture and slip distribution of the 17 August 1999 İzmit earthquake (*M* 7.4), North Anatolian fault, *Bull. Seismol. Soc. Am.* **92,** 43–60.

Bethmann, F., N. Deichmann, and P. M. Mai (2012). Seismic wave attenuation from borehole and surface records in the top 2.5 km beneath the city of Basel, Switzerland, *Geophys. J. Int.* **190,** 1257–1270.

Bindi, D., B. Petrovic, S. Karapetrou, M. Manakou, T. Boxberger, D. Raptakis, K. D. Pitilakis, and S. Parolai (2015). Seismic response of an 8-story RC-building from ambient vibration analysis, *Bull. Earthq. Eng.* **13,** 2095–2120.

Blakeslee, S., and P. Malin (1991). High-frequency site effects at two Parkfield downhole and surface stations, *Bull. Seismol. Soc. Am.* **81,** 332–345.

Bohnhoff, M., F. Bulut, G. Dresen, P. E. Malin, T. Eken, and M. Aktar (2013). An earthquake gap south of Istanbul, *Nat. Commun.* **4,** doi: 10.1038/ncomms2999.

Bohnhoff, M., H. Grosser, and G. Dresen (2006). Strain partitioning and stress rotation at the North Anatolian fault zone from aftershock focal mechanisms of the 1999 Izmit $M_w = 7.4$ earthquake, *Geophys. J. Int.* **166,** 373–385.

Bohnhoff, M., H.-P. Harjes, and T. Meier (2005). Deformation and stress regimes in the Hellenic subduction zone from focal mechanisms, *J. Seismol.* **9,** 341–366.

Bulut, F., M. Bohnhoff, M. Aktar, and G. Dresen (2007). Characterization of aftershock-fault plane orientations of the 1999 İzmit (Turkey) earthquake using high-resolution aftershock locations, *Geophys. Res. Lett.* **34,** L20306, doi: 10.1029/2007GL031154.

Bulut, F., M. Bohnhoff, W. L. Ellsworth, M. Aktar, and G. Dresen (2009). Microseismicity at the North Anatolian fault in the Sea of Marmara offshore Istanbul, NW Turkey, *J. Geophys. Res.* **114,** no. B09302.

Bulut, F., W. L. Ellsworth, M. Bohnhoff, M. Aktar, and G. Dresen (2011). Spatiotemporal earthquake clusters along the North Anatolian fault zone offshore İstanbul, *Bull. Seismol. Soc. Am.* **101,** 1759–1768.

Dey-Sarkar, S. K., and R. A. Wiggins (1976). Source deconvolution of teleseismic *P* wave arrivals between 14° and 40°, *J. Geophys. Res.* **81,** 3633–3641.

Dix, C. H. (1955). Seismic velocities from surface measurements, *Geophysics* **20,** 68–86.

Eken, T., M. Bohnhoff, F. Bulut, B. Can, and M. Aktar (2013). Crustal anisotropy in the eastern Sea of Marmara region in northwestern Turkey, *Bull. Seismol. Soc. Am.* **103,** 911–924.

Ergintav, S., R. E. Reilinger, R. Çakmak, M. Floyd, Z. Cakir, U. Doğan, R. W. King, S. McClusky, and H. Özener (2014). Istanbul's earthquake hot spots: Geodetic constraints on strain accumulation along faults in the Marmara seismic gap, *Geophys. Res. Lett.* **41,** 5783–5788.

Flerit, F., R. Armijo, G. King, and B. Meyer (2004). The mechanical interaction between the propagating North Anatolian fault and the back-arc extension in the Aegean, *Earth Planet. Sci. Lett.* **224,** 347–362.

Ge, J., J. Pujol, S. Pezeshk, and S. Stovall (2009). Determination of shallow shear-wave attenuation in the Mississippi embayment using vertical seismic profiling data, *Bull. Seismol. Soc. Am.* **99,** 1636–1649.

Gibbs, J. F., D. M. Boore, W. B. Joyner, and T. E. Fumal (1994). The attenuation of seismic shear waves in Quaternary alluvium in Santa Clara Valley, California, *Bull. Seismol. Soc. Am.* **84,** 76–90.

Gündüz, H., K.-Ö. Ayşe, B.-G. Aysun, and T. Niyazi (1998). S-wave attenuation in the Marmara Region, northwestern Turkey, *Geophys. Res. Lett.* **25,** 2733–2736.

Hauksson, E., T.-L. Teng, and T. L. Henyey (1987). Results from a 1500 m deep, three-level downhole seismometer array: Site response, low *Q* values, and f_{max}, *Bull. Seismol. Soc. Am.* **77,** 1883–1904.

Helmberger, D., and R. A. Wiggins (1971). Upper mantle structure of midwestern United States, *J. Geophys. Res.* **76,** 3229–3245.

Hubert-Ferrari, A., A. Barka, E. Jacques, S. S. Nalbant, B. Meyer, R. Armijo, P. Tapponnier, and G. C. P. King (2000). Seismic hazard in the Marmara Sea region following the 17 August 1999 Izmit earthquake, *Nature* **404,** 269–273.

Hurd, O., and M. Bohnhoff (2012). Stress and structural-induced shear-wave anisotropy along the 1999 Izmit rupture, northwest Turkey, *Bull. Seismol. Soc. Am.* **102,** no. 5, 2177–2188.

Kiratzi, A. A. (2002). Stress tensor inversions along the westernmost North Anatolian fault zone and its continuation into the North Aegean Sea, *Geophys. J. Int.* **151,** 360–376.

Leary, P. C., and F. Al-Kindy (2002). Power-law scaling of spatially correlated porosity and log (permeability) sequences from north-central North Sea Brae oilfield well core, *Geophys. J. Int.* **148,** 426–442.

Lienert, B. R., E. Berg, and L. N. Frazer (1986). HYPOCENTER: An earthquake location method using centered, scaled, and adaptively damped least squares, *Bull. Seismol. Soc. Am.* **76,** 771–783.

Malin, P. E., J. A. Waller, R. D. Borcherdt, E. Cranswick, E. G. Jensen, and J. V. Schaack (1988). Vertical seismic profiling of Oroville microearthquakes: Velocity spectra and particle motion as a function of depth, *Bull. Seismol. Soc. Am.* **78,** 401–420.

McClusky, S., S. Balassanian, A. Barka, C. Demir, S. Ergintav, I. Georgiev, O. Gurkan, M. Hamburger, K. Hurst, H. Kahle, *et al.* (2000). Global Positioning System constraints on plate kinematics and dynamics in the eastern Mediterranean and Caucasus, *J. Geophys. Res.* **105,** 5695–5719.

Mehta, K., R. Snieder, and V. Graizer (2007). Extraction of near-surface properties for a lossy layered medium using the propagator matrix, *Geophys. J. Int.* **169,** 271–280.

Nakata, N., and R. Snieder (2012). Estimating near-surface shear wave velocities in Japan by applying seismic interferometry to KiK-net data, *J. Geophys. Res.* **117,** no. B01308, doi: 10.1029/2011JB008595.

Özgül, N. (2012). Stratigraphy and some structural features of the İstanbul Palaeozoic, *Turkish J. Earth Sci.* **21,** 817–866.

Parolai, S., A. Ansal, A. Kurtulus, A. Strollo, R. Wang, and J. Zschau (2009). The Ataköy vertical array (Turkey): Insights into seismic wave propagation in the shallow-most crustal layers by waveform deconvolution, *Geophys. J. Int.* **178,** 1649–1662.

Parolai, S., D. Bindi, A. Ansal, A. Kurtulus, A. Strollo, and J. Zschau (2010). Determination of shallow *S*-wave attenuation by down-hole waveform deconvolution: A case study in Istanbul (Turkey), *Geophys. J. Int.* **181,** 1147–1158.

Parolai, S., M. Mucciarelli, M. R. Gallipoli, S. M. Richwalski, and A. Strollo (2007). Comparison of empirical and numerical site responses at the Tito test site, southern Italy, *Bull. Seismol. Soc. Am.* **97,** 1413–1431.

Parolai, S., R. Wang, and D. Bindi (2012). Inversion of borehole weak motion records observed in Istanbul (Turkey), *Geophys. J. Int.* **188,** 535–548.

Parsons, T. (2004). Recalculated probability of $M \geq 7$ earthquakes beneath the Sea of Marmara, Turkey, *J. Geophys. Res.* **109,** no. 5, doi: 10.1029/2003JB002667.

Prevedel, B., F. Bulut, M. Bohnhoff, C. Raub, R. Kartal, F. Alver, and P. Malin (2015). Downhole geophysical observatories: Best installation practices and a case history from Turkey, *Int. J. Earth. Sci.* **104,** 1–11, doi: 10.1007/s00531-015-1147-5.

Şafak, E. (1997). Models and methods to characterize site amplification from a pair of records, *Earthq. Spectra* **13,** 97–129.

Shearer, P. M., and J. A. Orcutt (1987). Surface and near-surface effects on seismic waves: Theory and borehole seismometer results, *Bull. Seismol. Soc. Am.* **77,** 1168–1196.

Shiomi, K., H. Sato, and M. Ohtake (1997). Broad-band power-law spectra of well-log data in Japan, *Geophys. J. Int.* **130,** 57–64.

Silva, M. B. C., and A. Stovas (2009). Comparison of averaging methods for velocity model building from well logs, *J. Geophys. Eng.* **6,** 172.

Snieder, R., and E. Şafak (2006). Extracting the building response using seismic interferometry: Theory and application to the Millikan Library in Pasadena, California, *Bull. Seismol. Soc. Am.* **96,** 586–598.

Steidl, J. H., A. G. Tumarkin, and R. J. Archuleta (1996). What is a reference site? *Bull. Seismol. Soc. Am.* **86,** 1733–1748.

Stein, R. S., A. A. Barka, and J. H. Dieterich (1997). Progressive failure on the North Anatolian fault since 1939 by earthquake stress triggering, *Geophys. J. Int.* **128,** 594–604.

Tibi, R., G. Bock, Y. Xia, M. Baumbach, H. Grosser, C. Milkereit, S. Karakisa, S. Zünbül, R. Kind, and J. Zschau (2001). Rupture processes of the 1999 August 17 Izmit and November 12 Düzce (Turkey) earthquakes, *Geophys. J. Int.* **144,** F1–F7.

Tonn, R. (1991). The determination of the seismic quality factor Q from VSP data: A comparison of different computational methods, *Geophys. Prospect.* **39,** 1–27.

Trampert, J., M. Cara, and M. Frogneux (1993). *SH* propagator matrix and Q_S estimates from borehole- and surface-recorded earthquake data, *Geophys. J. Int.* **112,** 290–299.

van Vossen, R., J. Trampert, and A. Curtis (2004). Propagator and wave-equation inversion for near-receiver material properties, *Geophys. J. Int.* **157,** 796–812.

Vasconcelos, I., and R. Snieder (2008a). Interferometry by deconvolution, Part 1: Theory for acoustic waves and numerical examples, *Geophysics* **73,** S115–S128.

Vasconcelos, I., and R. Snieder (2008b). Interferometry by deconvolution, Part 2: Theory for elastic waves and application to drill-bit seismic imaging, *Geophysics* **73,** S129–S141.

Wang, R. (1999). A simple orthonormalization method for stable and efficient computation of Green's functions, *Bull. Seismol. Soc. Am.* **89,** 733–741.

Appendix

Orientation of Downhole Horizontal Components

During the deployment of the downhole three-component geophones, the vertical component of the instruments follows the direction of the well path, which deviates from verticality by less than 2° (Prevedel *et al.*, 2015), whereas the orientation of the horizontal components cannot be controlled due to rotation of the instruments around their vertical axis while they are lowered into the hole. Therefore, before comparing the horizontal components of the surface and downhole sensors with each other, the downhole horizontal components need to be rotated into the same direction as the orientation of the surface components, that is, to the north and east directions.

The rotation angle is determined by calculating cross correlations between the horizontal components of the surface sensor with rotated horizontal components of the downhole sensor. Thereby the downhole sensor is clockwise rotated in 1° steps. The angle that yields the largest cross-correlation coefficient is regarded as the angle of deviation from north and east.

To avoid a false angle determination due to scattered high-frequency waves, we low-pass filtered the data below the first trough in the downhole spectra of the *P* and *S* waves at ∼3 Hz. Thus, for this analysis we had to select a second dataset of well-recorded regional and teleseismic events that have a sufficiently strong content of low-frequency energy. Eleven events with hypocentral distances between 114 and 1614 km and magnitudes of 4.7–6.4 were selected from the Kandilli Observatory and Earthquake Research Institute (KOERI) catalog. Because of their lack of high-frequency energy, these 11 events are not part of the dataset used in the shallow wave-propagation study.

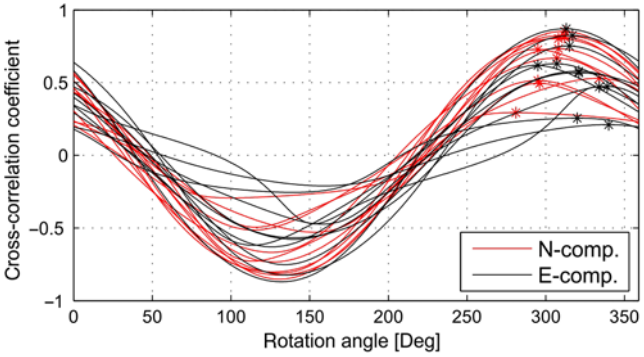

Figure A1. Cross-correlation functions of the 2 Hz geophone at 288 m depth from all 11 events that were selected for the orientation of the downhole horizontal components (N, north; E, east). The maximum cross-correlation coefficient is marked by a star. The color version of this figure is available only in the electronic edition.

For the cross-correlation analysis, we selected the whole signal (*P* and *S* waves) and used instrument-corrected recordings. The cross-correlation functions for all 11 events are presented in Figure A1. They are very coherent and thus present a stable result. Averaging the maximum cross-correlation coefficients yields the angle of deviation from north and east of 313° ± 15°. Thus, as the first processing step of the shallow wave-propagation study, the downhole horizontal components of the sensor at 288 m depth are clockwise rotated by 313°.

Helmholtz Centre Potsdam
GFZ German Research Centre for Geosciences
Section 4.2 Geomechanics and Rheology
Telegrafenberg
14473 Potsdam, Germany
craub@gfz-potsdam.de
(C.R., M.B.)

Helmholtz Centre Potsdam
GFZ German Research Centre for Geosciences
Centre for Early Warning, Helmholtzstraße 6/7
14473 Potsdam, Germany
(B.P., S.P.)

ASIR/HydroGeo Inc.
1311 Waterside Drive
Dallas, Texas 75218
(P.M.)

Prime Ministry Disaster & Emergency Management Authority (AFAD)
Kızılırmak Mah. Ufuk Üniversitesi Cad. Nu. 12
06510 Çukurambar, Söğütözü
Çankaya, Ankara, Turkey
(K.Y., R.F.K., T.K.)

Manuscript received 17 August 2015;
Published Online 24 May 2016

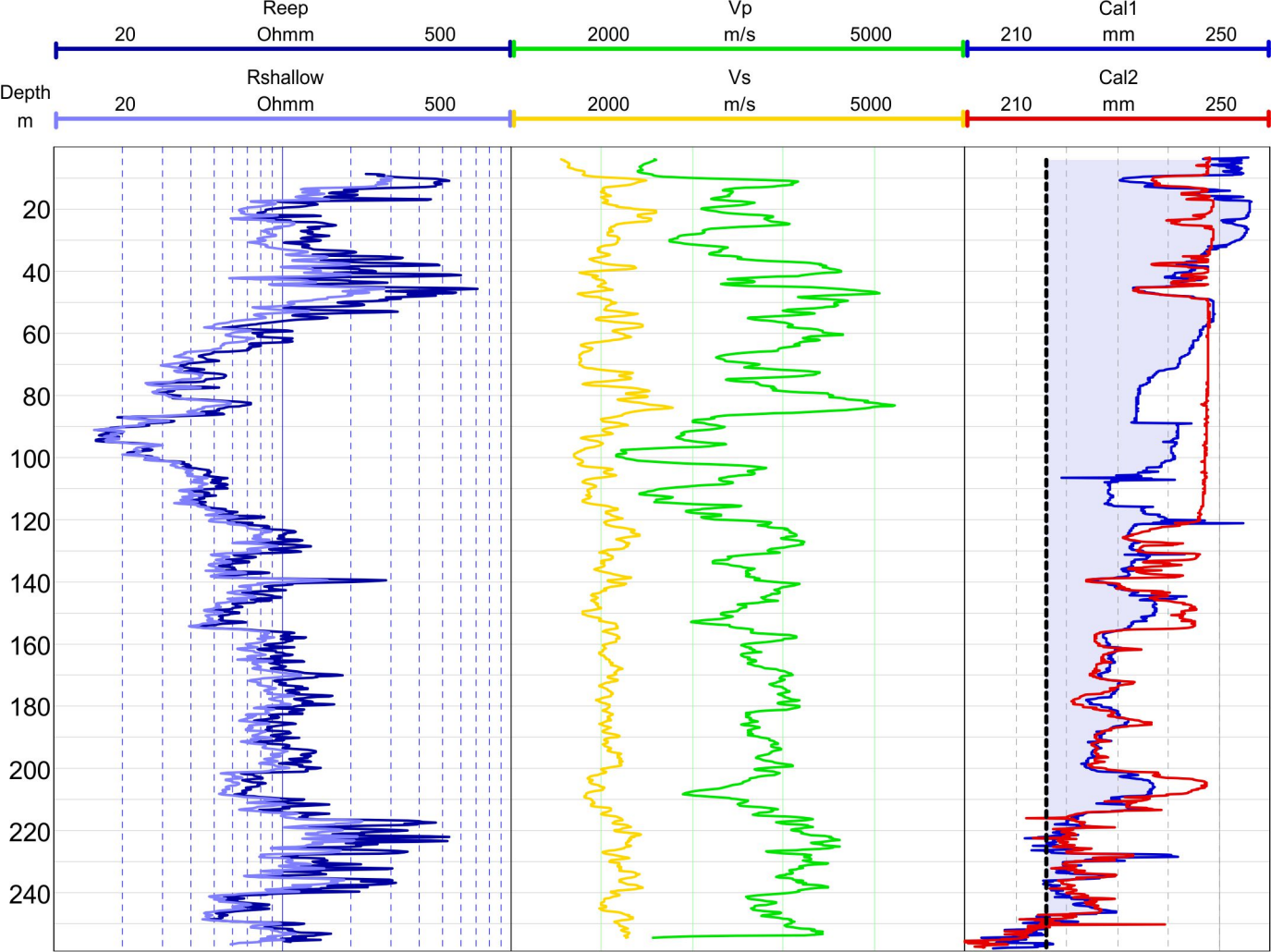
Reep
20
Ohmm
500
Vp
2000
m/s
5000
Cal1
210
mm
250
Depth
m
Rshallow
20
Ohmm
500
Vs
2000
m/s
5000
Cal2
210
mm
250
20
40
60
80
100
120
140
160
180
200
220
240

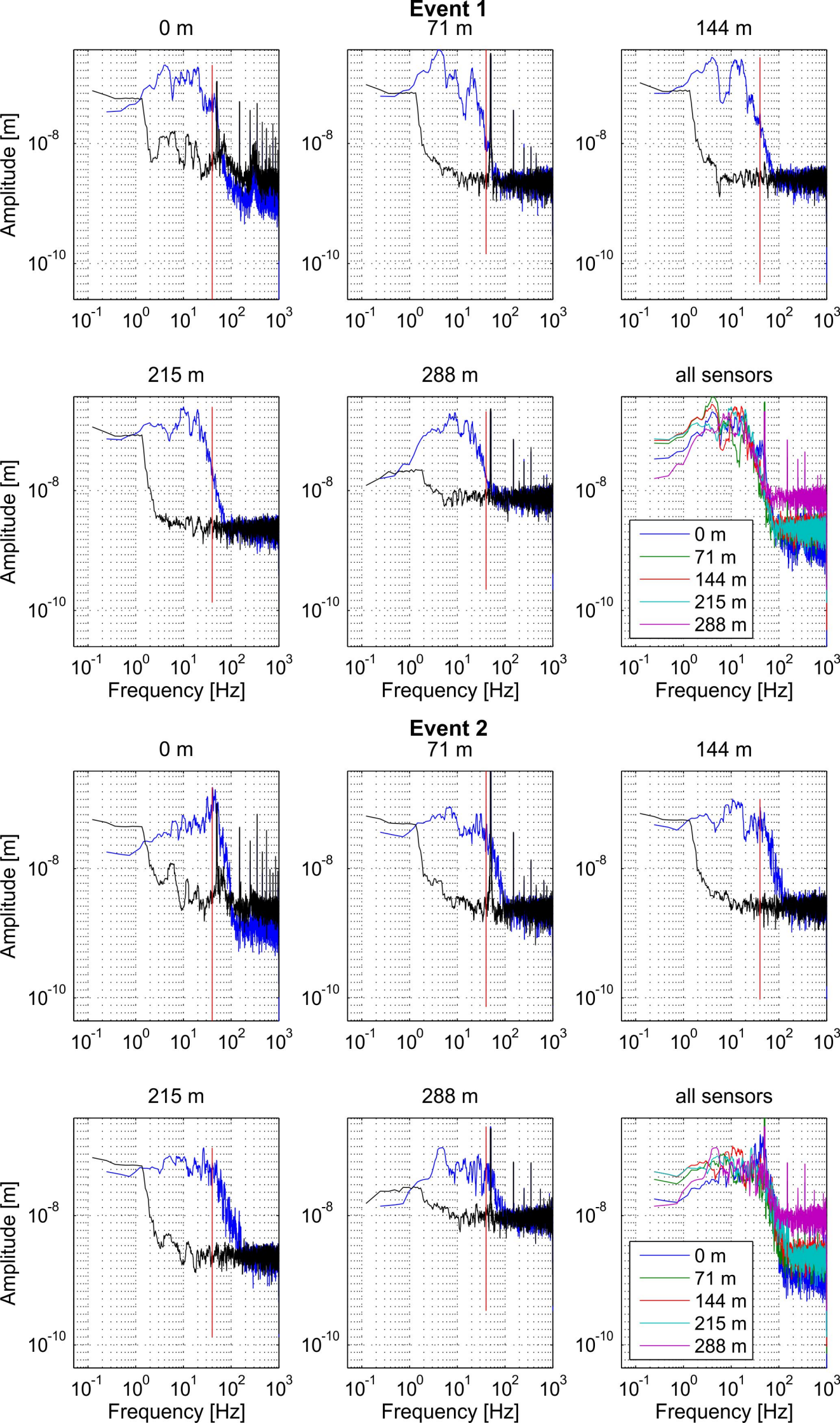
Event 1
0 m
71 m
144 m
215 m
288 m
all sensors
Amplitude [m]
Frequency [Hz]
0 m
71 m
144 m
215 m
288 m
Event 2
0 m
71 m
144 m
215 m
288 m
all sensors
Amplitude [m]
Frequency [Hz]
0 m
71 m
144 m
215 m
288 m

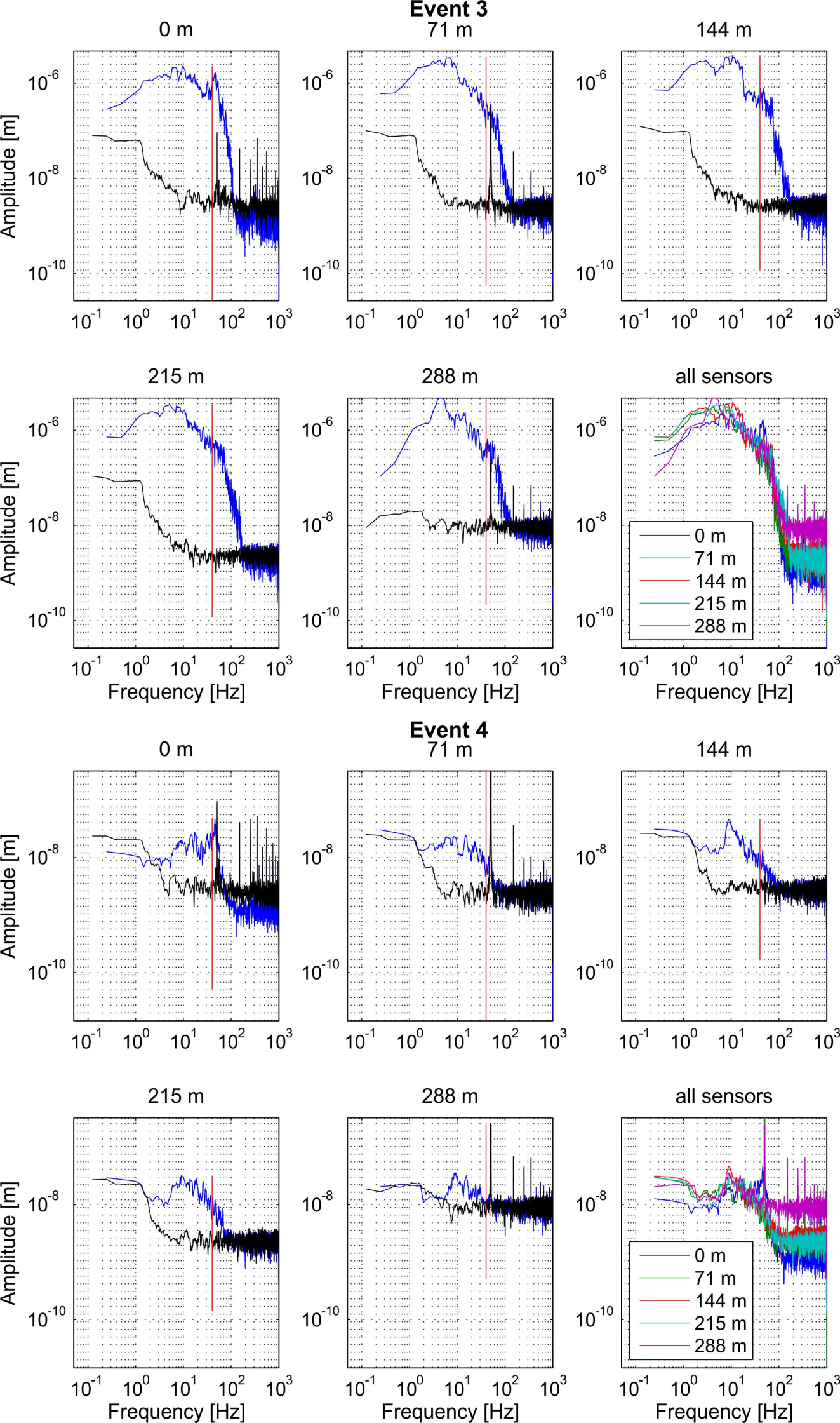
Event 3
0 m
71 m
144 m
215 m
288 m
all sensors
Amplitude [m]
Frequency [Hz]
0 m
71 m
144 m
215 m
288 m
Event 4
0 m
71 m
144 m
215 m
288 m
all sensors
Amplitude [m]
Frequency [Hz]
0 m
71 m
144 m
215 m
288 m

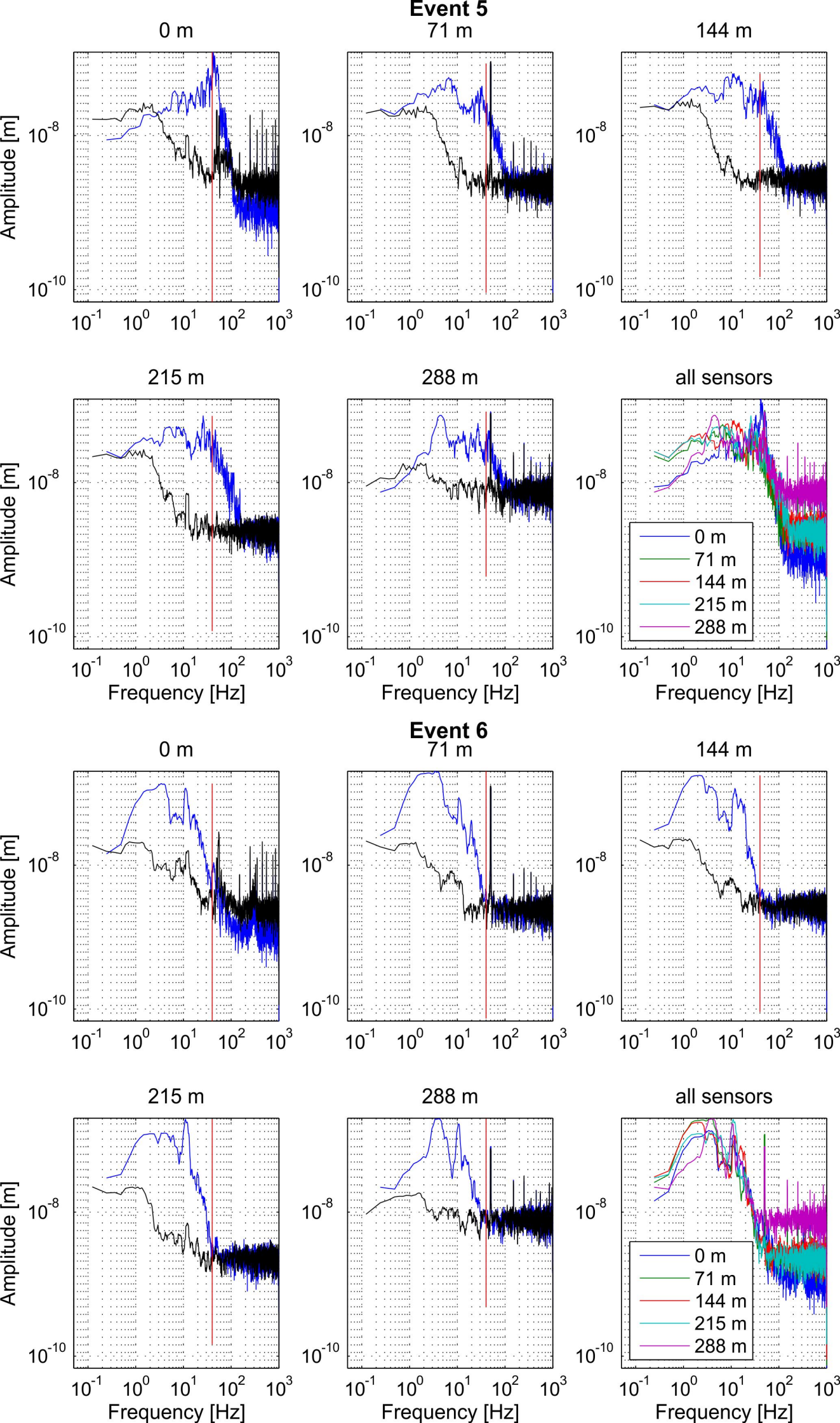
Event 5
0 m
71 m
144 m
215 m
288 m
all sensors
Amplitude [m]
Frequency [Hz]
0 m
71 m
144 m
215 m
288 m
Event 6
0 m
71 m
144 m
215 m
288 m
all sensors
Amplitude [m]
Frequency [Hz]
0 m
71 m
144 m
215 m
288 m

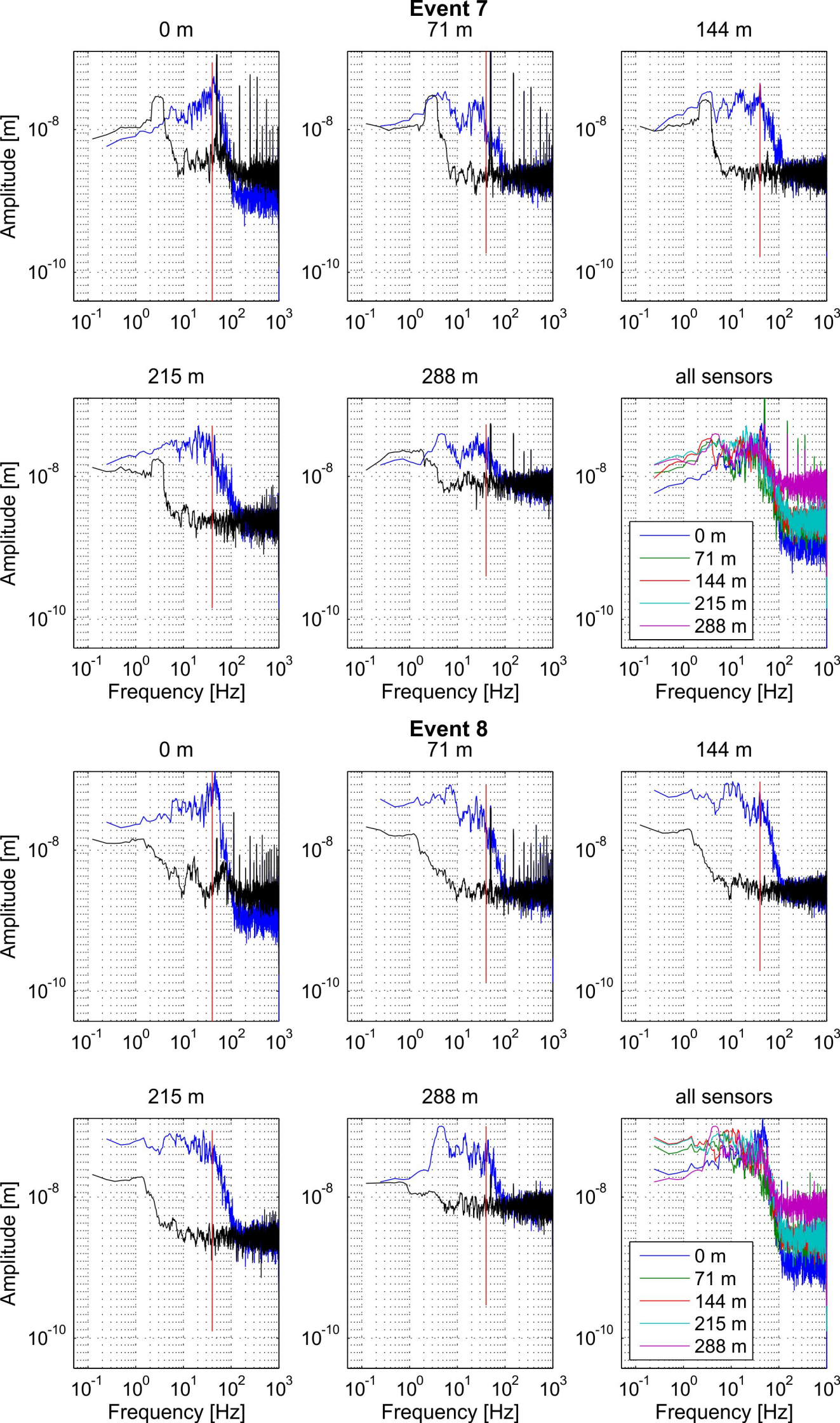
Event 7
0 m
71 m
144 m
215 m
288 m
all sensors
Amplitude [m]
Frequency [Hz]
0 m
71 m
144 m
215 m
288 m
Event 8
0 m
71 m
144 m
215 m
288 m
all sensors
Amplitude [m]
Frequency [Hz]
0 m
71 m
144 m
215 m
288 m

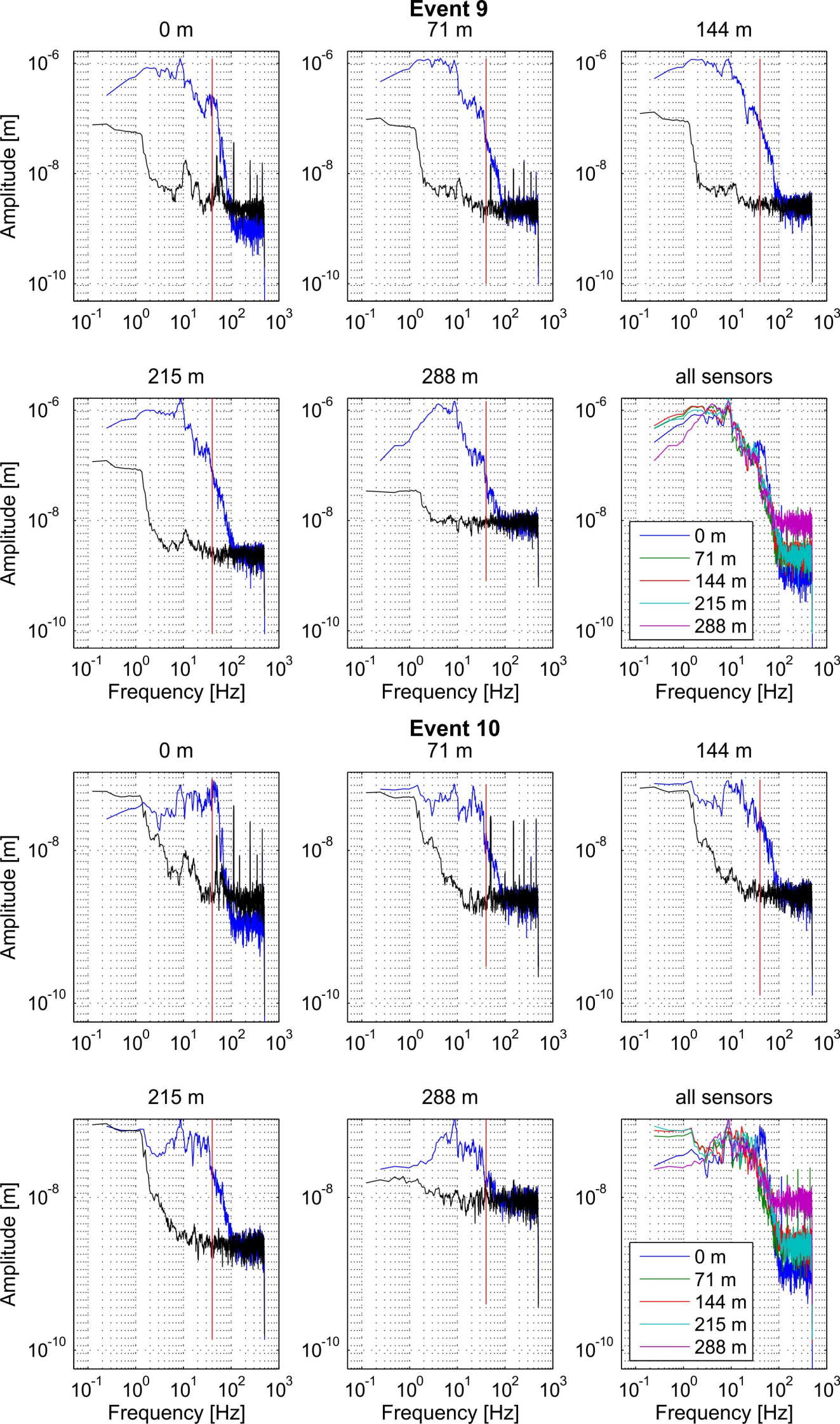
Event 9
0 m
71 m
144 m
215 m
288 m
all sensors
Amplitude [m]
Frequency [Hz]
0 m
71 m
144 m
215 m
288 m
Event 10
0 m
71 m
144 m
215 m
288 m
all sensors
Amplitude [m]
Frequency [Hz]
0 m
71 m
144 m
215 m
288 m

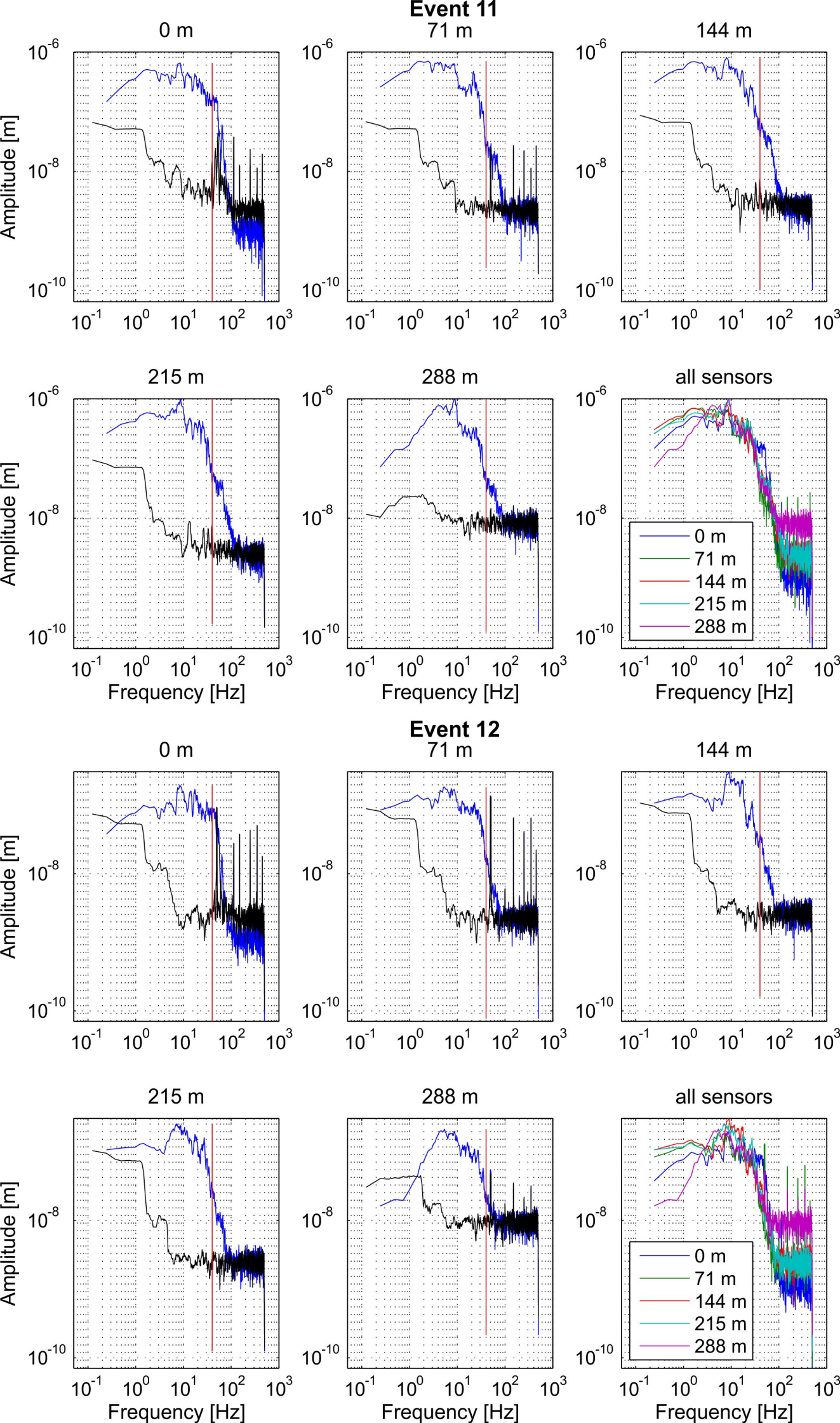
Event 11
0 m
71 m
144 m
215 m
288 m
all sensors
Amplitude [m]
Frequency [Hz]
0 m
71 m
144 m
215 m
288 m
Event 12
0 m
71 m
144 m
215 m
288 m
all sensors
Amplitude [m]
Frequency [Hz]
0 m
71 m
144 m
215 m
288 m

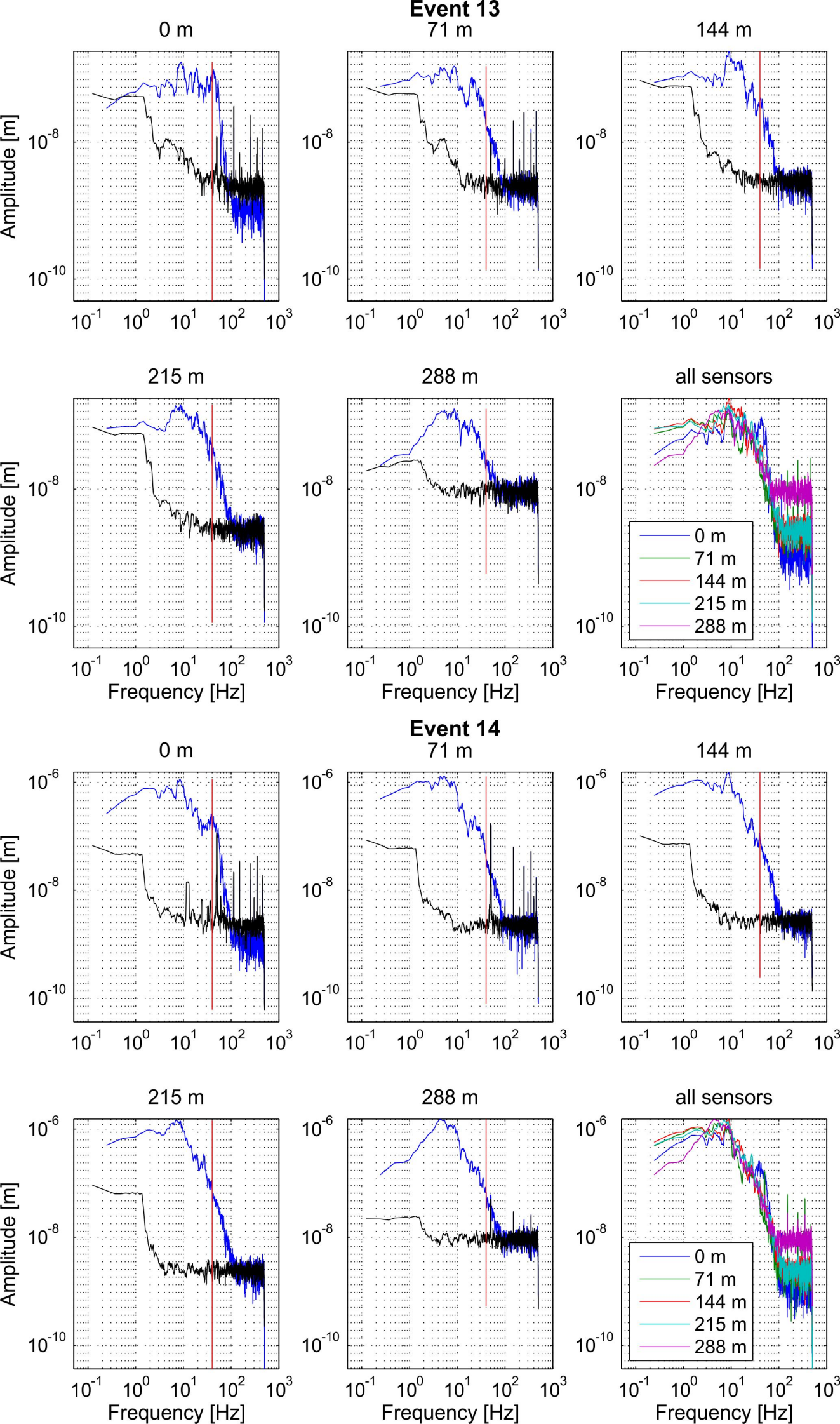
Event 13
0 m
71 m
144 m
215 m
288 m
all sensors
Amplitude [m]
Frequency [Hz]
0 m
71 m
144 m
215 m
288 m
Event 14
0 m
71 m
144 m
215 m
288 m
all sensors
Amplitude [m]
Frequency [Hz]
0 m
71 m
144 m
215 m
288 m

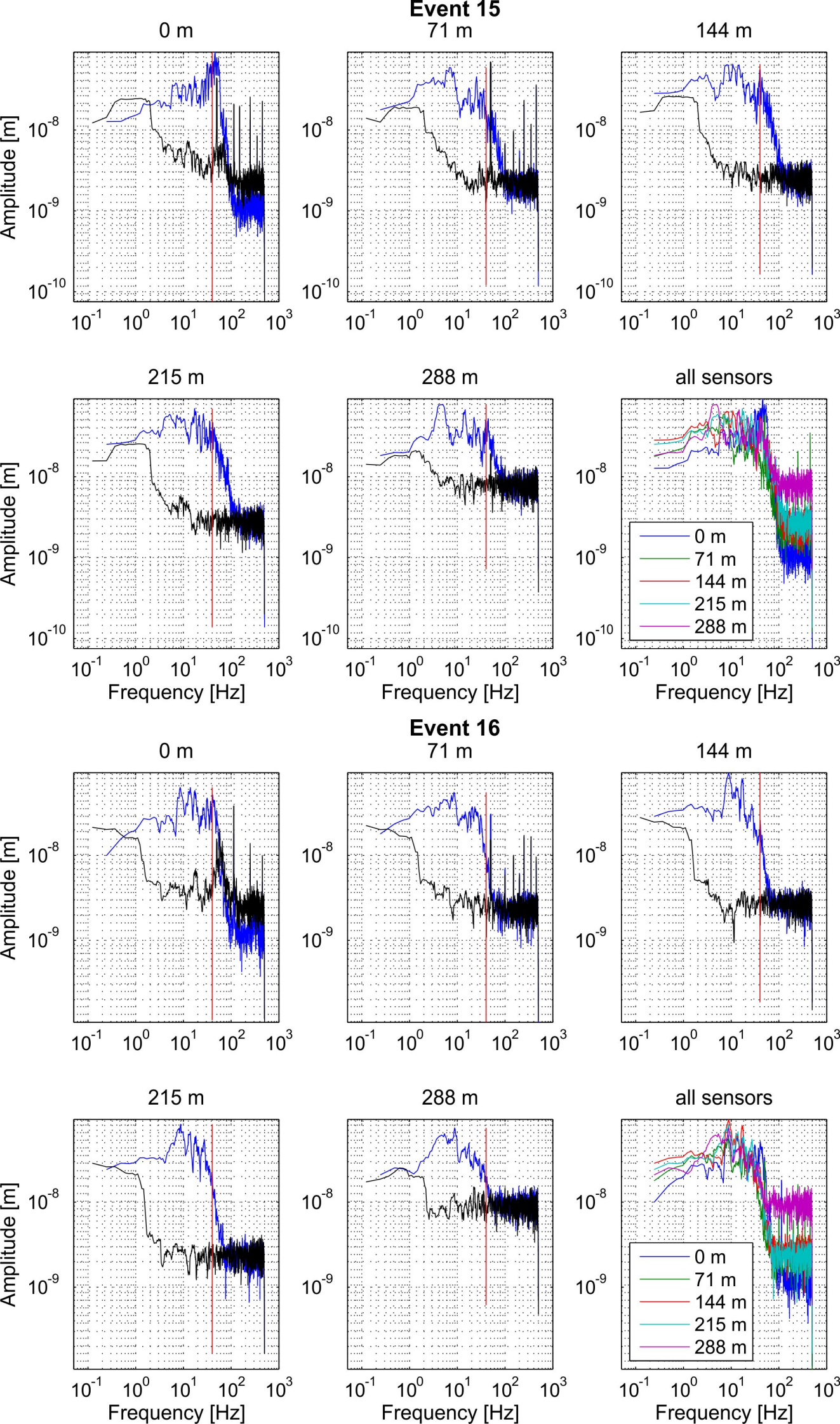
Event 15
0 m
71 m
144 m
215 m
288 m
all sensors
Amplitude [m]
Frequency [Hz]
0 m
71 m
144 m
215 m
288 m
Event 16
0 m
71 m
144 m
215 m
288 m
all sensors
Amplitude [m]
Frequency [Hz]
0 m
71 m
144 m
215 m
288 m

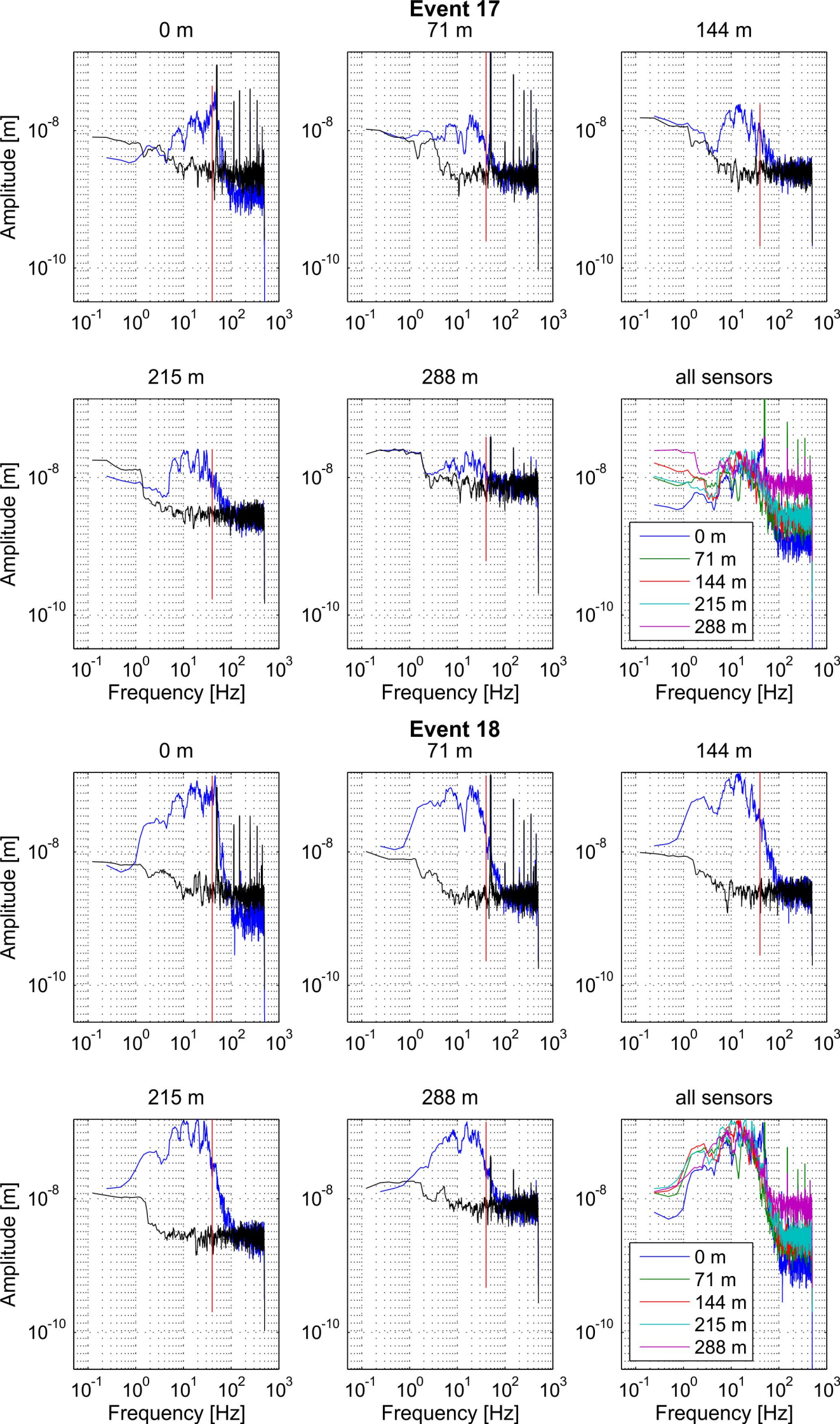
Event 17
0 m
71 m
144 m
215 m
288 m
all sensors
Amplitude [m]
Frequency [Hz]
0 m
71 m
144 m
215 m
288 m
Event 18
0 m
71 m
144 m
215 m
288 m
all sensors
Amplitude [m]
Frequency [Hz]
0 m
71 m
144 m
215 m
288 m

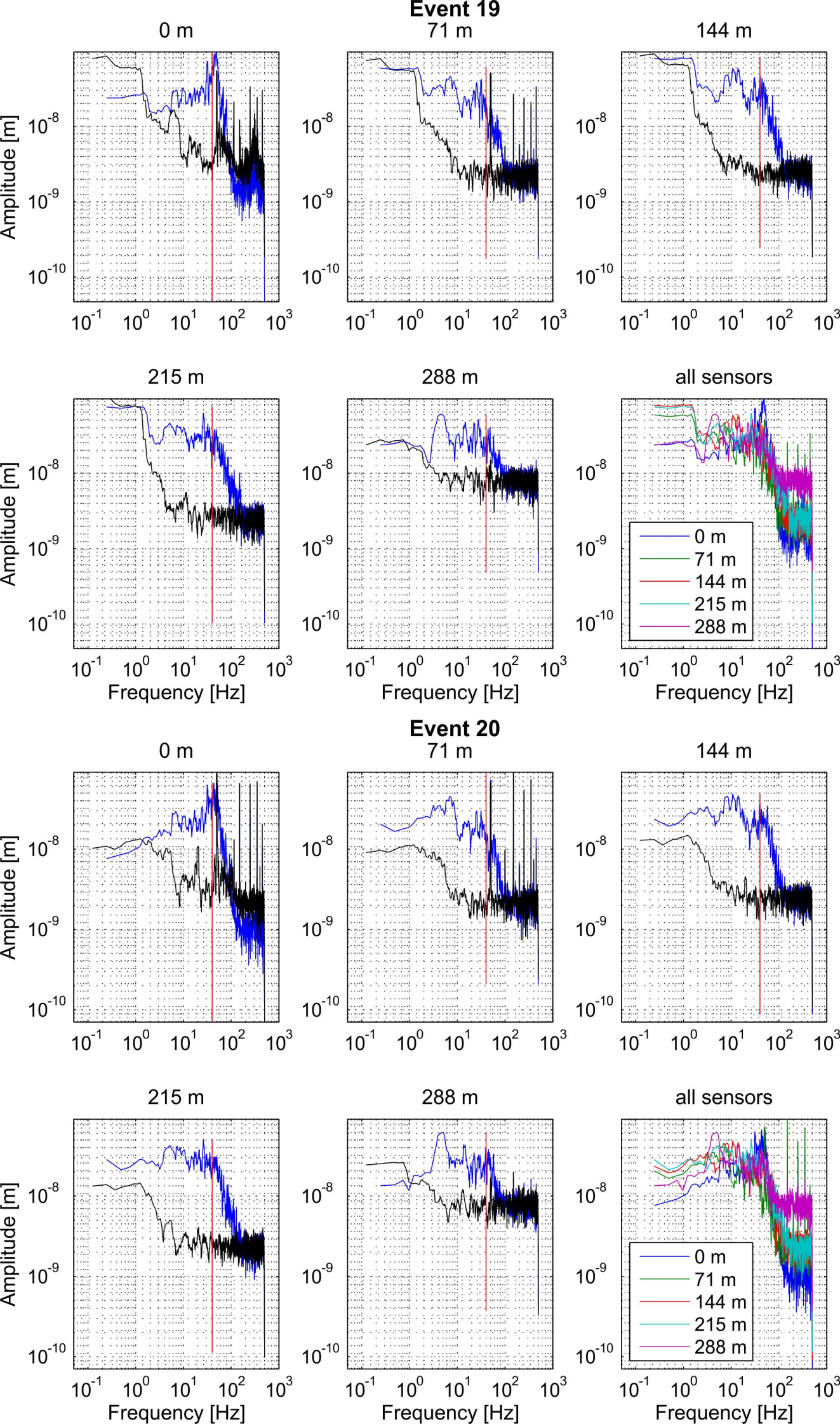
Event 19
0 m
71 m
144 m
215 m
288 m
all sensors
Amplitude [m]
Frequency [Hz]
0 m
71 m
144 m
215 m
288 m
Event 20
0 m
71 m
144 m
215 m
288 m
all sensors
Amplitude [m]
Frequency [Hz]
0 m
71 m
144 m
215 m
288 m

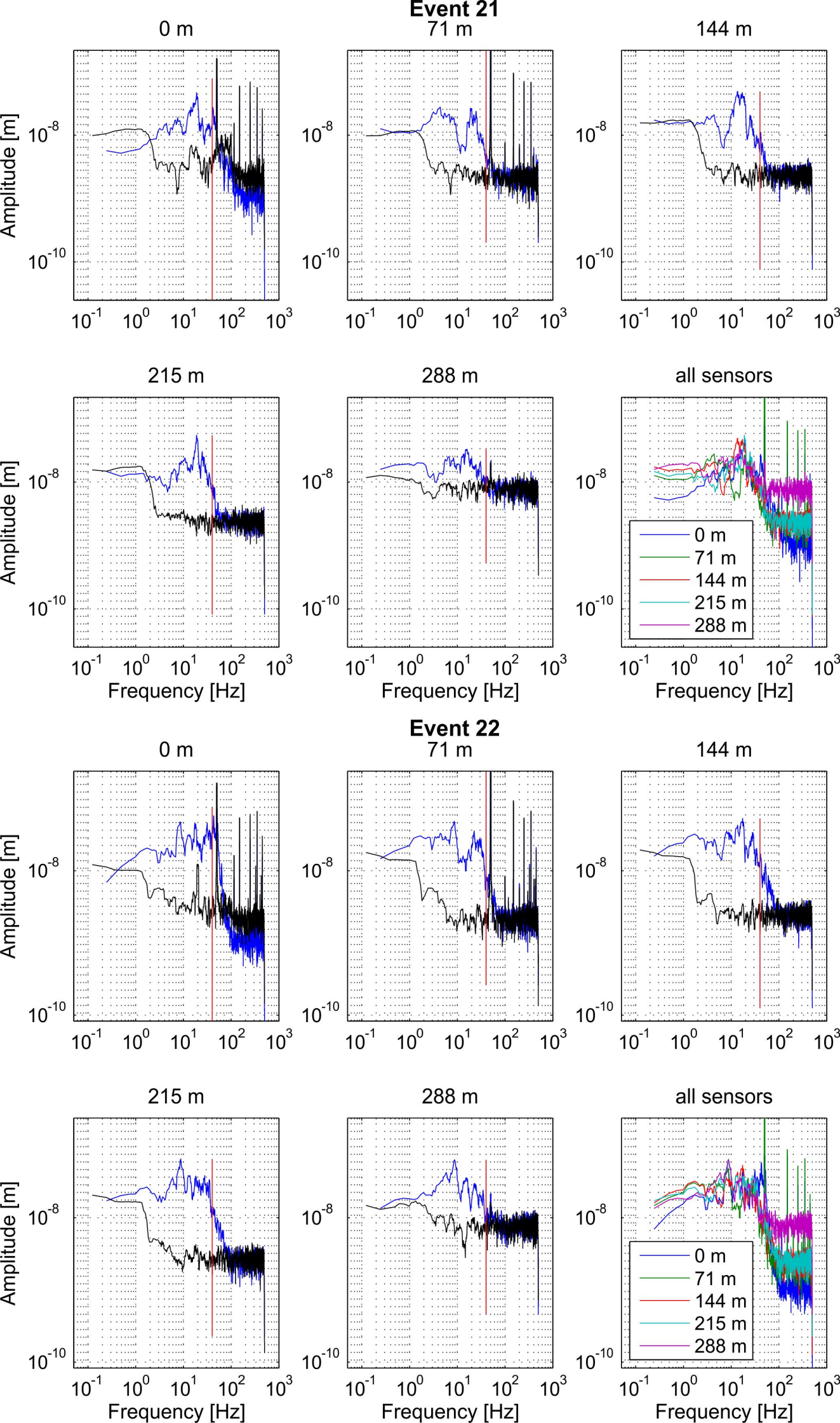
Event 21
0 m
71 m
144 m
215 m
288 m
all sensors
Amplitude [m]
Frequency [Hz]
0 m
71 m
144 m
215 m
288 m
Event 22
0 m
71 m
144 m
215 m
288 m
all sensors
Amplitude [m]
Frequency [Hz]
0 m
71 m
144 m
215 m
288 m

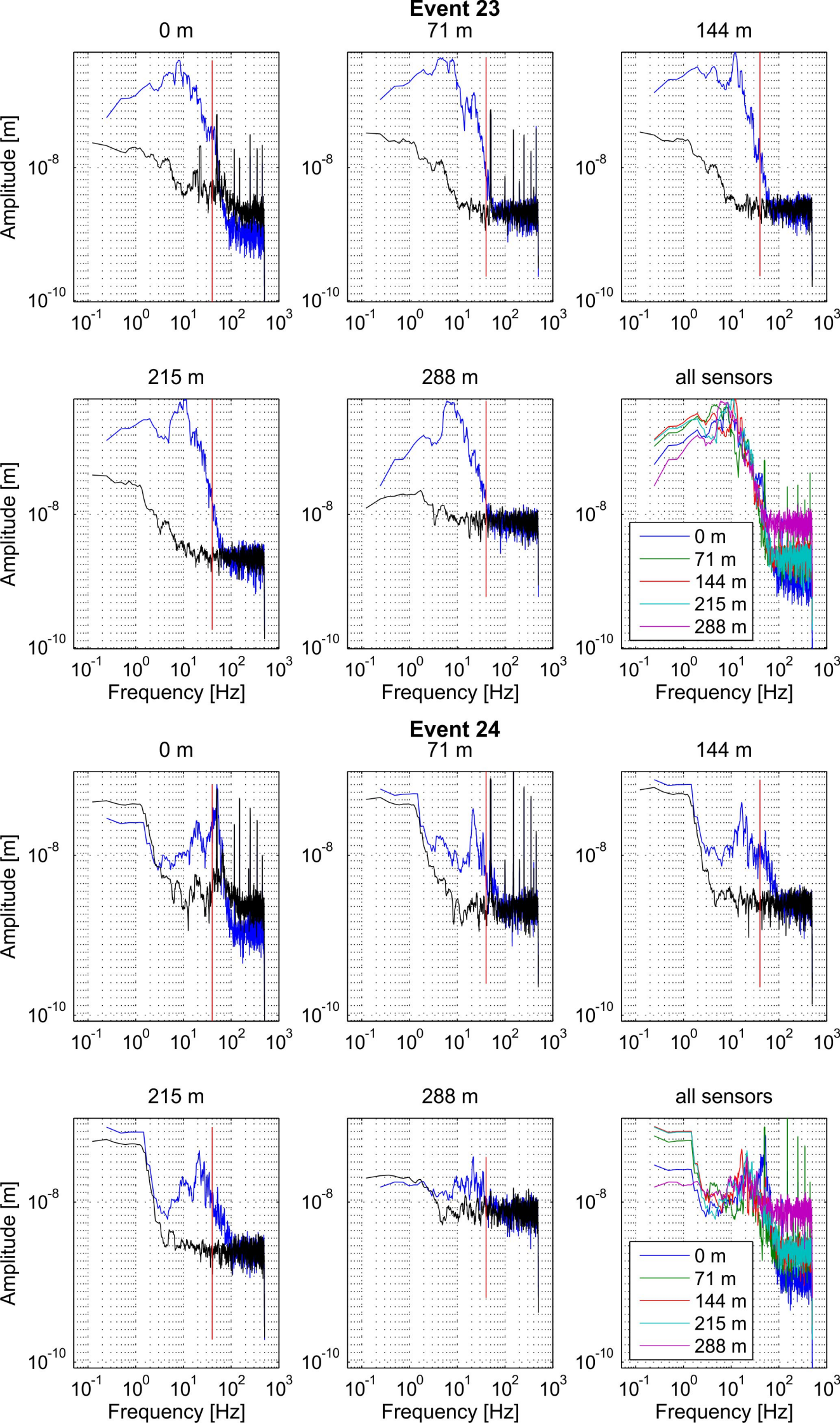
Event 23
0 m
71 m
144 m
215 m
288 m
all sensors
Amplitude [m]
Frequency [Hz]
0 m
71 m
144 m
215 m
288 m
Event 24
0 m
71 m
144 m
215 m
288 m
all sensors
Amplitude [m]
Frequency [Hz]
0 m
71 m
144 m
215 m
288 m

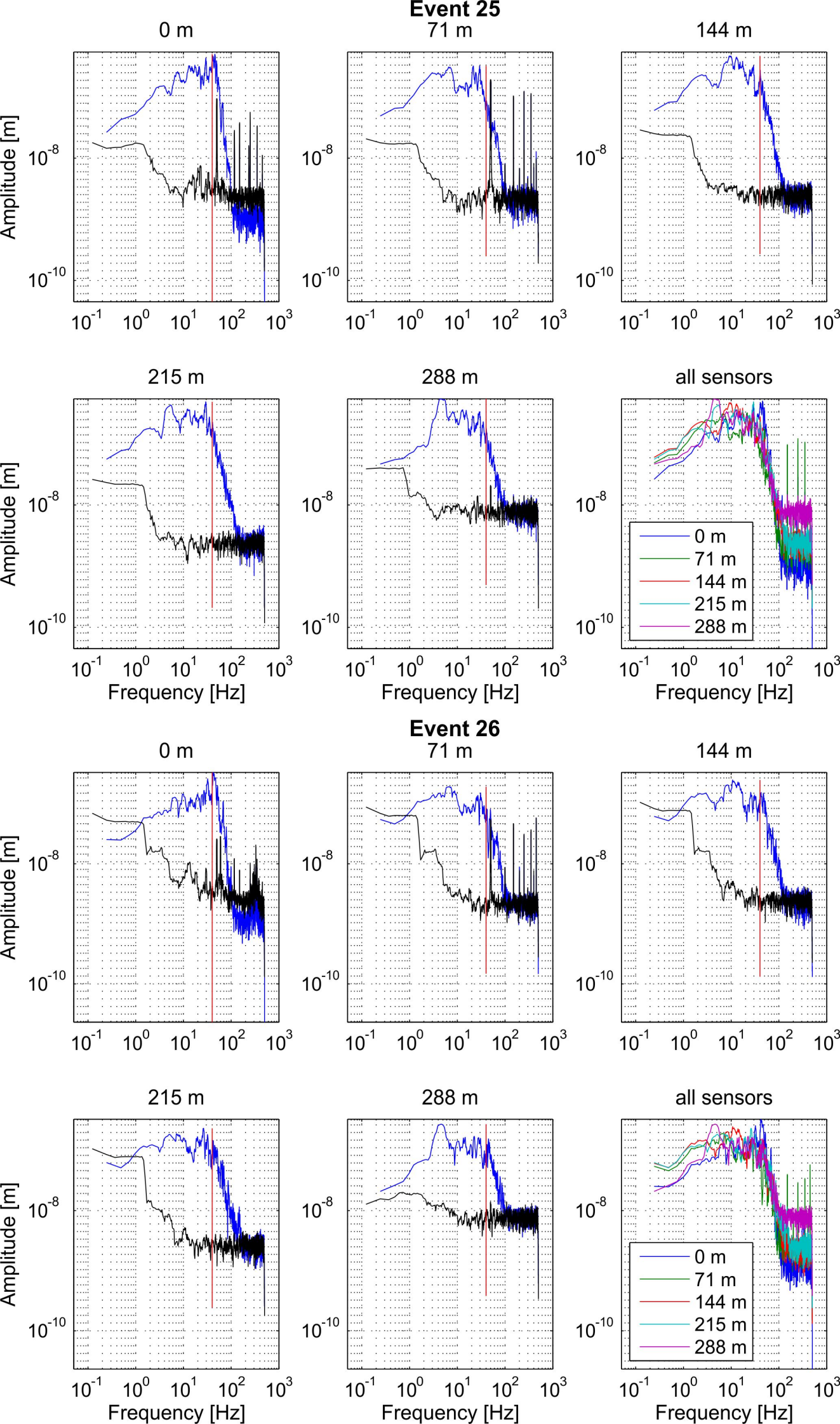
Event 25
0 m
71 m
144 m
215 m
288 m
all sensors
Amplitude [m]
Frequency [Hz]
0 m
71 m
144 m
215 m
288 m
Event 26
0 m
71 m
144 m
215 m
288 m
all sensors
Amplitude [m]
Frequency [Hz]
0 m
71 m
144 m
215 m
288 m